SAR Raw Data Simulation for Ocean Scenes Using Inverse Omega-K Algorithm

Baochang Liu and Yijun He, *Member, IEEE*

Abstract—This paper deals with synthetic aperture radar (SAR) raw data simulation for ocean scenes featuring surface waves and currents, an issue which has proven to be of great necessity in preparing for future oceanic SAR missions. In this paper, the inverse Omega-K (IOK) algorithm, which is originally designed for SAR raw data simulation of stationary land scenes, is extended to ocean scenes. To realize such a generalization, endeavors are made in two aspects. First, specially aimed at ocean dynamics of ocean waves and currents, the 2-D spectrum of the SAR signal is derived. Second, to account for the spatial variation of ocean-motion parameters, we adopt a strategy called batch processing, whose basic feature is that a single implementation of the IOK algorithm will simultaneously simulate a collection of ocean-surface backscattering elements that have the same radial velocity. For the proposed simulator, the velocity bunching effect is embodied via making the long-wave radial orbital velocities physically enter the range equation of the SAR raw signal, instead of superimposing this effect onto the reflectivity map. The spread of the facet velocities within one resolution cell enters the raw data through a random perturbation of the local long-wave orbital velocity. The proposed simulator is not only rather accurate due to the fact that, in deriving the range frequency mapping function, no Taylor expansion is made on the range equation, but also much more efficient than its time-domain counterpart. Effectiveness of the proposed simulator is validated by using simulation results.

Index Terms—Inverse Omega-K (IOK) algorithm, ocean scenes, ocean-surface currents, ocean-surface waves, synthetic aperture radar (SAR), synthetic aperture radar raw data simulation.

I. INTRODUCTION

A. Background of Ocean SAR Data Simulation

IN ORDER to effectively extract the oceanographic information contained in synthetic aperture radar (SAR) data (e.g., information on ocean internal waves, surface waves, surface currents, surface wind, etc. [1]–[6]), individual retrieval algorithms have to be developed. To this end, dealing with real-measured SAR data may serve as a direct way. However, in the response of a SAR to the continuously moving ocean surface (in contrast to the stationary land scene), there typically exist many complicated physical modulation processes, including the tilt modulation, the hydrodynamic modulation, the Doppler-shift modulation, the current-related modulation, etc. [7]–[13]. These processes are usually inseparably mixed together and interact between each other, thus posing some difficulties to the development of individual ocean-feature retrieval algorithms. Fortunately, such a limitation sometimes can be overcome by using *simulation* procedures [14], [15]. This is because simulation allows us to generate canonical ocean scenarios: By adjusting the input parameters to the simulator, we can respectively turn on or turn off certain modulation processes so that simulation can be used as a valuable aid in better understanding the complicated SAR imaging mechanisms of the ocean surface, proposing new ocean-feature retrieval algorithms, and further comparing different retrieval algorithms. Therefore, ocean SAR simulation is a necessary complement to real SAR data processing. Moreover, ocean SAR simulation is of great necessity in planning and preparing for future oceanic SAR missions [16]–[20]; The simulation tool would be used to optimize sensor configurations and to identify the optimal radar system parameters.

In general, ocean SAR simulation can be separated into two groups: the SAR image-based simulation and the SAR raw data simulation. For the first group, ocean SAR data are simulated at the image level: By using a certain formula, SAR imagery is numerically computed. For the second group, ocean SAR data are simulated at the source level: Such simulated ocean data correspond to those received onboard by the radar antenna before any processing. These data are referred to as SAR raw data. Up to now, the SAR image-based simulation (the first simulation group) has been intensively investigated in a large amount of literature [14], [15], [21]–[48]. By contrast, the studies on the ocean SAR raw data simulation (the second simulation group) are relatively few in the open literature to our knowledge. Two representative SAR raw data simulators for ocean scenes can be found in [49] and [50], which were developed by Franceschetti *et al.* based on Harger's DS model [25], [28], [37].

Although very useful in understanding SAR imaging mechanisms of ocean surfaces, the SAR image-based simulation is still shown to suffer from some drawbacks.

1) The image-based simulation shows its limitation whenever SAR focusing algorithms are to be proposed, developed, and tested [50].
2) Some useful information, e.g., the Doppler centroid, which has been widely used to retrieve ocean currents [51], [52], is usually missing in the data generated by image-based simulators.

3) Depending on the image-based simulation alone is usually not enough to develop pattern recognition techniques for ocean-surface feature extraction, e.g., oil slick detection. This is because the image-based simulator usually only provides the second moment of the SAR image intensity, but higher order statistics of the SAR image intensity is required to discriminate the features caused by oil slick from those originating from the lack of wind [50].

4) The existing image-based simulators ignore some SAR signal characteristics, e.g., Doppler aliasing due to the presence of Doppler components that lie outside the Doppler baseband, the cross coupling between range and azimuth, etc. All these SAR signal characteristics may have some effects on the retrieval of ocean-surface features.

By contrast, the ocean SAR raw data simulation does not suffer from the aforementioned limitations. This fact can be explained like this: The SAR raw data are simulated from the very beginning of the receiving of the radar echoes; in other words, the ocean SAR raw data simulation is a complete one, but the image-based simulation is not. Therefore, simulation of SAR raw data is highly desirable in the research area of oceanic remote sensing. From now on, we focus our attention on the ocean SAR raw data simulation.

B. Challenges in Developing a Simultaneously Computationally Efficient, Functionally Comprehensive, and Accurate SAR Raw Data Simulator for Ocean Scenes

Typically, there are at least three requirements that a good SAR raw data simulator should meet: functional comprehensiveness, efficiency, and accuracy. Functional comprehensiveness is related to the fact that the scene to be simulated should be an extended one (rather than a point-like scatterer), quite general (contains as many scene features as possible), and possibly time and/or space varying [53]. By efficiency, we mean that the implementation of the simulator should be fast and computer-memory saving. As far as the accuracy of the simulator is concerned, the raw data generated by the simulator should be as close to its real-measured counterpart as possible, given the same radar system parameters and the scene parameters.

According to the aforementioned criteria, SAR raw data simulators can be categorized into two classes: time-domain simulators and frequency-domain simulators. The first class [54]–[66], which works by a twofold summation of the individual impulse response functions of scattering elements weighted by their corresponding backscattering coefficients in the 2-D time domain (the azimuth time and range time domain), can exactly handle arbitrary radar trajectories and arbitrary scenes. This characteristic makes time-domain simulators very comprehensive and very accurate. However, one serious disadvantage of the time-domain simulators is that they are enormously time-consuming such that they are not useful in practice whenever extended scenes are to be simulated [67]. To overcome this drawback, frequency-domain simulators (the second class) were developed [67]–[87]. For such simulators, the SAR raw data are generated in the frequency domain by employing fast Fourier transform (FFT) instead of the twofold summation, thus making the frequency-domain simulators much more efficient

than the time-domain ones. Of particular interest among all frequency-domain simulators is the inverse Omega-K (IOK) algorithm [78], [82], [84], [86], an inverse version of a commonly used SAR imaging algorithm called the Omega-K algorithm [88], [89] whose key is the Stolt interpolation [90] according to the 2-D spectrum of the complex SAR signal. Because no approximation, except for the one required for the principle of stationary phase (POSP), is made when implementing the Stolt interpolation, the IOK algorithm can introduce the spatial variation of range–azimuth coupling and azimuth modulation exactly, which makes this simulator more accurate than other frequency-based simulators [82], [84]. Therefore, the IOK algorithm may be preferable to other SAR raw data simulators when one is concerned about both the accuracy and the efficiency of the simulation.

At present, the technique for simulating SAR raw data of stationary land scenes is rather mature, and a great deal of work can be found in the literature [53]–[87]. By contrast, this is not the case for the simulation of ocean SAR raw data. To the best of our knowledge, only Franceschetti *et al.* [49], [50] have systematically treated the issue of 2-D SAR raw data generation for ocean scenes. Although very computationally efficient, Franceschetti's simulators are, unfortunately, subject to some limitations in functional comprehensiveness. First, Franceschetti's ocean simulators, as specifically pointed out in [49], do not account for the velocity bunching (VB) effect, a phenomenon of the presence of wave-like patterns on the SAR image even in the hypothetical case when no modulation of the radar backscattering cross section by long ocean waves is present [11], [12].[1] Second, a *stochastic process* associated with the spread of radial velocities of the backscattering facets within a SAR resolution cell, is not involved in Franceschetti's simulators. Third, Franceschetti's simulators were not designed to aim to those ocean scenes where ocean-surface currents are present. Furthermore, as far as the accuracy is concerned, the performance of Franceschetti's ocean simulators also needs to be improved. In fact, these simulators rely on a frequency-domain raw data simulator called Synthetic Aperture Radar Advanced Simulator (SARAS) [53], for which, some approximations were made when deriving the interpolation formula.[2] Such approximations may degrade the accuracy of Franceschetti's ocean simulators to some extent. Therefore, endeavors are still needed to adequately simulate the SAR raw data for ocean scenes.

To overcome the limitations of the existing ocean SAR raw data simulators, one may conceive the idea of applying the IOK algorithm, which was originally used for SAR raw data simulation of stationary land scenes [78], [82], [84], [86], to ocean SAR raw data simulation since, just as stated earlier, this simulator is more accurate than other frequency-domain simulators. However, a difficulty arises when doing so: The motion parameters of the ocean waves are spatially varying, but the IOK algorithm

---

[1]The VB effect, whose existence has been confirmed by realistic experimental results [91], is generated through the modulation of alternating concentration and spreading of backscattering facets on the image plane due to the spatial variation in the radial orbital velocities associated with the long ocean waves [12].

[2]According to [82] and [84], SARAS [53] can be considered an inverse procedure of the chirp scaling imaging algorithm [92] for which some approximations were introduced when formulating this algorithm.

requires all parameters involved in the frequency mapping function to remain spatially constant. Such a contradiction makes it not straightforward to directly apply the IOK algorithm to ocean SAR raw data simulation.

To sum up, in order to develop an ocean SAR raw data simulator that is simultaneously computationally efficient, functionally comprehensive, and accurate, there are three technical questions which remain to be tackled.

1) Can the VB effect be physically embodied via using long-wave orbital velocities as input parameters to the simulator, instead of at the image level as done in most of SAR image-based simulators?
2) Can the spread of the radial facet velocities within a SAR resolution cell enter the SAR raw data physically and directly, rather than by means of making such a stochastic process equivalent to an effect of azimuth-resolution degradation?
3) Can the computational efficiency of the IOK algorithm [82], when applied to ocean scenes, be exploited to some extent, although the full computational efficiency is difficult to obtain?

C. Objectives and Contributions of This Paper

This paper aims to answer the aforementioned questions. Specifically, we have two objectives. The first objective, which is treated in Section II, is related to the issue of how to physically incorporate into an ocean SAR raw data simulator the phenomenon of VB as well as the stochastic process of radial velocity spread of the backscattering facets on the subresolution scale. As our second objective, we make an attempt to generalize the IOK algorithm [82], which was originally designed for the stationary land scenes, to a new version that can address the ocean scenes featuring ocean-surface waves and currents. Sections III and IV discuss the second objective in detail.

II. OCEAN SAR RAW DATA FORMULA IN THE 2-D TIME DOMAIN

This section is intended to formulate the specific expression for the SAR raw data of ocean scenes in the 2-D time domain. Although not very useful in practical applications because of its high computational complexity, such a time-domain ocean SAR raw data formula is still of theoretical significance in the following two aspects: First, this formula can shed light on the issue of how to embody the VB effect at the physical level (instead of at *a posteriori* level); second, this formula serves as a preliminary to the development of a new version of the IOK algorithm to be discussed in Section III. To facilitate the discussion, let us first give the ocean scene/SAR geometry.

A. Ocean Scene/SAR Geometry

To begin with the description, we consider a right-hand Cartesian coordinate system, as shown in Fig. 1, where the xy plane is locally tangent to the surface of the Earth. In this coordinate system, a SAR system, working in the stripmap mode with a zero squint, is assumed flying on a straight track parallel to the x-axis, with a platform velocity of v and an altitude of H.
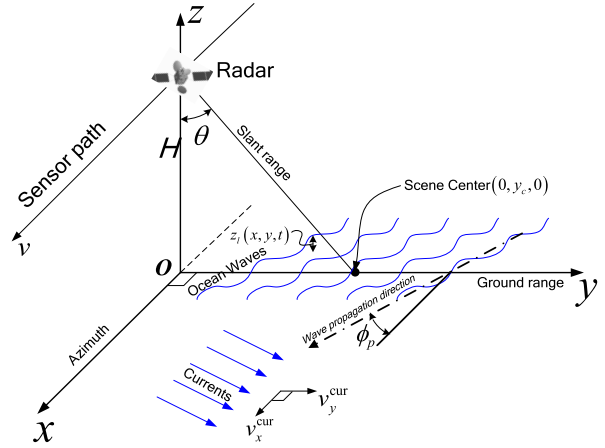

Fig. 1. SAR/ocean scene geometry.

The flight path of the radar platform is on the xz plane. The x-axis and y-axis are referred to as azimuth and ground-range coordinates, respectively. Suppose that an ocean scene featuring both surface waves and currents is illuminated by the SAR. The scene center is chosen to be located at coordinate $(0, y_c, 0)$, with y_c being the ground-range coordinate of the ocean scene center.

B. Ocean-Surface Modeling

The formulation of an ocean SAR raw data simulator involves the modeling of the ocean surface. A widely acknowledged ocean-surface model is the two-scale composite model [93], with the ocean-surface waves divided into *long* waves and *short* waves via a separation wavelength typically set to be an order of magnitude larger than the wavelength of the incident electromagnetic wave. In order to account for the particularities of ocean SAR raw data simulation, it is necessary to adapt the separation scale of this two-scale model. In this paper, we choose the separation scale to be the *pixel* dimension of SAR images. Accordingly, we divide the entire ocean surface into individual backscattering facets with each facet having a dimension equal to that of a SAR pixel, so that the *discrete* coordinates of the ocean surface in azimuth and ground ranges, which are consistent with the coordinate system shown in Fig. 1, can be respectively expressed as

$$x_m = \Delta x(m - M/2)|_{m=1,2,...,M} \tag{1}$$
$$y_n = y_c + \Delta y(n - N/2)|_{n=1,2,...,N} \tag{2}$$

where M and N are the numbers of facets in azimuth and ground range, respectively, and Δx and Δy are the SAR pixel sizes in azimuth and ground range, respectively, which are expressed as

$$\Delta x = \frac{v}{\text{PRF}} \tag{3}$$
$$\Delta y = \frac{c}{2 \cdot F_s \cdot \sin(\theta)} \tag{4}$$

with PRF being the pulse repetition frequency of the radar, F_s the range sampling rate of the radar, c the speed of light, and θ the incidence angle. In simulating the ocean SAR raw data, ocean waves longer than the SAR pixel scale, consisting mainly of gravity waves, are treated deterministically, whereas subpixel scale waves, consisting mainly of gravity–capillary and capillary waves, are treated statistically. Note that the short

waves are superimposed on the long waves and modulated by these long waves.

1) Description of Wave Profile: According to [38], the long wave height field at spatial coordinate (x_m, y_n) and time t may be written as

$$z_l(x_m, y_n, t) = \iint \xi_{k_x,k_y} \cos(k_x \cdot x_m + k_y \cdot y_n - \omega_{k_x,k_y} \cdot t + \psi_{k_x,k_y}) dk_x dk_y \quad (5)$$

where the subscript "l" means "long wave," and k_x and k_y represent the azimuth wavenumber and range wavenumber coordinates of ocean waves, respectively. The angular frequency ω_{k_x,k_y} of a deep-water ocean wave is related to its wavenumber vector (k_x, k_y) via the following dispersion relationship [94]:

$$\omega_{k_x,k_y} = \sqrt{g \cdot \sqrt{k_x^2 + k_y^2}} \quad (6)$$

where g is the gravity acceleration. In (5), the phase ψ_{k_x,k_y} is uniformly distributed over $(0, 2\pi)$, and the amplitude ξ_{k_x,k_y} is taken according to the long-wave spectral density through the following expression:

$$\xi_{k_x,k_y} = \sqrt{E_l(k_x, k_y)}/\xi_0 \quad (7)$$

where $E_l(k_x, k_y)$ denotes the long-wave spectral density at (k_x, k_y), and ξ_0 is a normalization factor that is chosen such that $z_l(x, y, t)$ yields the prescribed value of the significant wave height H_s shown as follows:

$$\sqrt{\langle z_l^2 \rangle} = H_s/4 \quad (8)$$

with $\sqrt{\langle z_l^2 \rangle}$ being the root mean square (rms) surface height. With regard to the specific form of the long-wave spectral density, we adopt, in this paper, the JONSWAP spectrum [44], [95], whose specific expression is given in Appendix I.

Concerning the short ocean wave height field $z_s(x_m, y_n, t)$ of scales smaller than one SAR pixel, we model it as a stochastic process whose wave spectral density is chosen to be the Phillips spectrum [11], as given by

$$E_s(k_x, k_y) = \beta \left(\sqrt{(k_x)^2 + (k_y)^2} \right)^{-4} \quad (9)$$

where the subscript "s" means "short wave," and β is the Phillips parameter describing the intensity of the short wave spectrum.

2) Modulation of Normalized Radar Cross Section: Having described the ocean wave height field, we now delineate the interaction between the incoming electromagnetic wave and the ocean surface. Here, we consider a widely recognized backscattering mechanism, i.e., the Bragg resonance scattering [12], [49] which is valid for intermediate incidence angles from $20°$ to $70°$, a typical angle range in which SAR systems are operated [12]. For this backscattering mechanism, the radar cross section (RCS) is modulated by the ocean waves via two effects: the tilt modulation and the hydrodynamic modulation. The tilt modulation is solely related to the geometric effect that the radar illuminates the ocean waves at different local incident angles, whereas the hydrodynamic modulation is caused by a nonuniform distribution of the Bragg scattering waves (short

waves) along the long ocean wave profile due to interactions between short and long waves. The normalized RCS (NRCS) associated with these two modulations for horizontal/horizontal (HH) polarization at coordinate (x_m, y_n), can be expressed as

$$\sigma_{HH}^0(x_m, y_n, t) = \kappa_{\text{hydr}}(x_m, y_n, t) \cdot \sigma_{HH_{\text{tilt}}}^0(x_m, y_n, t) \quad (10)$$

where $\sigma_{HH_{\text{tilt}}}^0(x_m, y_n, t)$ denotes the NRCS originating from the tilt modulation and $\kappa_{\text{hydr}}(x_m, y_n, t)$ is the modulation factor pertaining to the hydrodynamic modulation. The specific expression for $\sigma_{HH_{\text{tilt}}}^0(x_m, y_n, t)$ was derived in [11] and is shown in Appendix II. Following the way adopted in [37], [49], and [50], we can account for the hydrodynamic modulation via the following:

$$\kappa_{\text{hydr}}(x_m, y_n, t) = 1 + z_l(x_m, y_n, t) \cdot k_p \quad (11)$$

where k_p is the wavenumber of the dominant wave component of the ocean scene.

3) Motion Characteristics of the Ocean Surface: According to ocean wave theories, for deep water waves, water particles on the ocean surface are moving around circular orbits [7]. Suppose that, as shown in Fig. 1, long ocean waves with a dominant wave component traveling off the azimuth direction by an angle of ϕ_p, are superimposed on an ocean-surface current which has an azimuth velocity component of v_x^{cur} and a ground-range velocity component of v_y^{cur}.

Now, let us formulate a velocity vector $\mathbf{v}_{1\times2}$ on the slant-range plane (see Fig. 1) to describe the motions of the long waves and the current, shown as $\mathbf{v}_{1\times2} = [v_x(x_m, y_n, t), v_r(x_m, y_n, t)]$, where $v_x(x_m, y_n, t)$ and $v_r(x_m, y_n, t)$ are azimuth and the radial velocity fields of the ocean surface, respectively. Following the derivation in [7] and [38], and making a consistency with the ocean-surface height field $z_l(x_m, y_n, t)$ shown in (5), we can express $v_r(x_m, y_n, t)$ as

$$v_r(x_m, y_n, t) = v_y^{\text{cur}} \cdot \sin\left(\text{atan}\left(\frac{y_n}{H}\right)\right)$$
$$+ \iint \xi_{k_x,k_y} \omega_{k_x,k_y} g_{k_x,k_y} \cos$$
$$(k_x x_m + k_y y_n - \omega_{k_x,k_y} t + \psi_{k_x,k_y} + \psi_v) dk_x dk_y \quad (12)$$

where the first term is the radial component of the current velocity, and the second term is the radial long-wave orbital velocity field, with g_{k_x,k_y} and ψ_v respectively expressed as

$$g_{k_x,k_y} = \sqrt{\left(k_y/\sqrt{k_x^2+k_y^2}\right)^2 \sin^2(\theta(y_n)) + \cos^2(\theta(y_n))} \quad (13)$$

$$\psi_v = \text{atan}\left(\frac{\sqrt{k_x^2 + k_y^2} \cdot \cos(\theta(y_n))}{k_y \cdot \sin(\theta(y_n))}\right). \quad (14)$$

In (13) and (14), the incidence angle θ is a function of the ground-range coordinate y_n of the ocean scene (see Fig. 1), as given in (63). As for the expression for $v_x(x_m, y_n, t)$, we have

$$v_x(x_m, y_n, t) = v_x^{\text{cur}}. \quad (15)$$

Note that, in (15), we neglect the azimuth velocities of the long waves since they are far less than the radar platform velocity.

Based on the discussion in [13], the short-wave related motions within one SAR pixel can be modeled as a random

Gaussian distribution with expectation zero and standard deviation (std) $\sqrt{\langle (u_r^{\mathrm{pix}})^2 \rangle}$. The specific expression for $\sqrt{\langle (u_r^{\mathrm{pix}})^2 \rangle}$, which was derived in [44], takes the following form:

$$\sqrt{\left\langle \left(u_r^{\mathrm{pix}} \right)^2 \right\rangle} = \sqrt{\frac{\beta \cdot g \cdot \sqrt{\Delta x \cdot \Delta y}}{2\pi}} \quad (16)$$

where u_r^{pix} is a random variable characterizing the distribution of the radial velocities of short waves within one SAR pixel. It should be noted that the expression for $\sqrt{\langle (u_r^{\mathrm{pix}})^2 \rangle}$ shown in (16) slightly differs from its original version derived in [44], in that, in (16), the SAR *pixel* dimension is used, whereas in [44, Eq. (5)], the SAR resolution dimension was adopted. These modifications stems from the fact that the separation scale dividing the ocean waves is chosen, in this paper, to be the SAR pixel dimension, for the sake of the ocean SAR raw data simulation.

C. Representation of Ocean SAR Raw Data in the 2-D Time Domain

1) Generation of the Reflectivity Map: To proceed with our discussion, we shall specify two hypotheses. The first one is that the NRCS varies a little over the SAR illumination time. This hypothesis is usually justified for cases when the SAR illumination time is small compared with the period of the dominant ocean wave. In fact, this hypothesis has been adopted in [48] and [96]. Based on such a hypothesis, we can neglect the time dependence of $\sigma_{HH}^0(x_m, y_n, t)$ in (10), so that the NRCS can be simply written as $\bar{\sigma}_{HH}^0(x_m, y_n)$ by inserting $t = (x_m/v - v_x^{\mathrm{cur}})$ into $\sigma_{HH}^0(x_m, y_n, t)$, i.e.,

$$\bar{\sigma}_{HH}^0(x_m, y_n) = \sigma_{HH}^0(x_m, y_n, t)|_{t=\frac{x_m}{v-v_x^{\mathrm{cur}}}}. \quad (17)$$

The second hypothesis is that the complex reflectivity of spatially separated facets are mutually uncorrelated, meaning that the complex reflectivity $\gamma(x_m, y_n)$ at coordinate (x_m, y_n) and the one $\gamma(x_l, y_q)$ at (x_l, y_q) satisfy the following relation:

$$E\left[\gamma(x_m, y_n) \cdot (\gamma(x_l, y_q))^*\right] = \bar{\sigma}_{HH}^0(x_m, y_n) \\ \cdot \delta(m-l) \cdot \delta(n-q) \quad (18)$$

where $E[\cdot]$ denotes the expectation operator, the superscript "$*$" means complex conjugate, $\delta(\cdot)$ is a delta function, and m, n, l, and q are all integers. Note that the hypothesis given by (18) has been confirmed by experimental results [97]. Based on the two aforementioned hypotheses, the random complex reflectivity $\gamma(x_m, y_n)$ at (x_m, y_n) can be generated via a random number generator, shown as

$$\gamma(x_m, y_n) = \aleph_{mn} \quad (19)$$

where $\aleph_{mn}$ is a complex circular Gaussian random number, with its expectation set to be zero and its variance set to be $\bar{\sigma}_{HH}^0(x_m, y_n)$. Note that the Gaussian random numbers $\{\aleph_{mn}\}$ for different facets are independently generated so that (18) is satisfied.

2) Simplification of the Ocean-Surface Radial Velocity Field: As shown in (12), the ocean-surface radial velocity field is time dependent, imposing some difficulties on the ocean SAR raw data simulation. Thus, it is necessary to simplify this radial ve-

locity field. To this end, let us expand $v_r(x_m, y_n, t)$ into Taylor series around the time $t = (x_m/v - v_x^{\mathrm{cur}})$, just as done in [48] and [96]. Retaining terms up to the second order, we have

$$v_r(x_m, y_n, t) = v_r^0(x_m, y_n) + a_r(x_m, y_n)\left(t - \frac{x_m}{v-v_x^{\mathrm{cur}}}\right) \quad (20)$$

where

$$v_r^0(x_m, y_n) = v_r(x_m, y_n, t)|_{t=\frac{x_m}{v-v_x^{\mathrm{cur}}}} \quad (21)$$

and $a_r(x_m, y_n)$ denotes the radial orbital acceleration associated with the long waves, as given by

$$a_r(x_m, y_n) = \iint \xi_{k_x, k_y} \omega_{k_x, k_y}^2 g_{k_x, k_y} \sin\left(k_x x_m \\ + k_y y_n - \omega_{k_x, k_y} \frac{x_m}{v-v_x^{\mathrm{cur}}} + \psi_{k_x, k_y} + \psi_v\right) dk_x dk_y. \quad (22)$$

Note that the presence of $a_r(x_m, y_n)$ will lead to a certain degree of *variation* in the radial velocity during the SAR illumination time T_a. On the other hand, the Gaussian random variable u_r^{pix} [see (16)] is also related to a kind of radial velocity spread (variation). In addition, a_r and u_r^{pix} can both cause a degradation in azimuth resolution of the SAR image. Thus, based on such similarity, we consider also modeling the velocity variation due to the radial orbital acceleration to be a Gaussian *random* velocity,[3] $u_r^{\mathrm{acc}}(x_m, y_n)$, with expectation zero and std, i.e.,

$$\sqrt{\left\langle (u_r^{\mathrm{acc}})^2 \right\rangle}(x_m, y_n) = a_r(x_m, y_n) \cdot T_a. \quad (23)$$

Then, we can combine $u_r^{\mathrm{acc}}(x_m, y_n)$ and u_r^{pix} into one random variable, as shown in the following:

$$u_r(x_m, y_n) = u_r^{\mathrm{acc}}(x_m, y_n) + u_r^{\mathrm{pix}}. \quad (24)$$

Following an assumption that the motion processes of long waves and short waves are independent, we can evaluate the std of u_r as follows:

$$\sqrt{\langle u_r^2 \rangle}(x_m, y_n) = \sqrt{\left\langle (u_r^{\mathrm{acc}})^2 \right\rangle + \left\langle \left(u_r^{\mathrm{pix}} \right)^2 \right\rangle}. \quad (25)$$

3) Combination of Subpixel Scale Wave Velocity Distribution into Long-Wave Orbital Velocity: In many of the SAR image-based ocean-surface simulators, e.g., in [12], [13], [44], and [48], the spread of the radial facet velocities within one resolution cell was made equivalent to a degradation in the azimuth resolution. However, doing so imposes some limitations on the simulated SAR data: The *randomness* feature of the velocity spread is impaired to some extent; moreover, the random Doppler fluctuations of backscattered signals in the Doppler domain cannot be embodied. To overcome these limitations, herein, we adopt an alternative strategy: Implement a *perturbation* on the local facet radial velocity associated with

---

[3]Another reason for doing so is that if the long-wave-related orbital acceleration is directly involved into the range equation [see (27) in Section II-C4], then the derivation of the 2-D spectrum of the ocean SAR signal (see Section III-B) would become rather difficult (if not impossible).
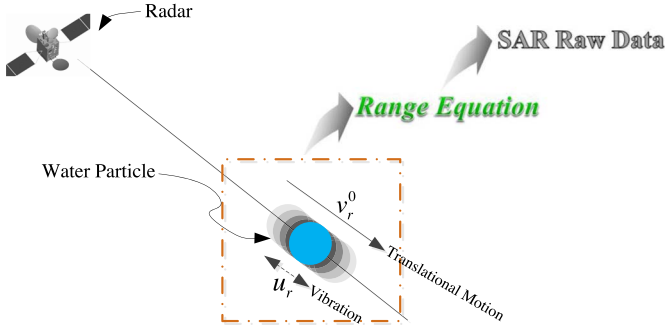
Fig. 2. Illustration of how the ocean dynamics enter SAR raw data. A backscattering facet is modeled to be a simultaneously translational moving and vibrating water particle. Then, the dynamics of this particle enters directly the range equation of the SAR signal and finally enters the SAR raw data.

the long waves and the current, by using a *random* variable related to the subpixel (subfacet) scale wave motions. To be more specific, we combine $u_r(x_m, y_n)$ [see (24)] into $v_r^0(x_m, y_n)$ [see (21)] so that a new radial velocity field of the ocean surface can be obtained, i.e.,

$$\widehat{v}_r(x_m, y_n) = v_r^0(x_m, y_n) + u_r(x_m, y_n). \qquad (26)$$

The physical implication of (26) is that, by means of the perturbation, a backscattering facet on the ocean surface is modeled to be a simultaneously *translational moving* and *vibrating* water particle with a mean velocity component of $v_r^0(x_m, y_n)$ and a random velocity component of $u_r(x_m, y_n)$, as shown in Fig. 2. The spatially uncorrelated random velocity $u_r(x_m, y_n)$ at position (x_m, y_n) can be generated by a Gaussian random number generator with its mean set to be zero and its std set to be $\sqrt{\langle u_r^2 \rangle}(x_m, y_n)$ [see (25)], just as done in generating $\gamma(x_m, y_n)$ [see (18) and (19)].

4) Incorporation of Ocean Dynamics into the Range Equation: As discussed in Section I, the long-wave orbital-velocity-related VB effect plays an important role in the ocean SAR imaging mechanism. For the SAR-image-based ocean scene simulators [4], [7], [11]–[14], [23], [44], [48], the VB effect is directly embodied at the SAR image level using a numerical evaluation. In [39], superimposing the VB effect on the reflectivity map was suggested. However, all these methods are not applicable to ocean SAR raw data simulation since the aim of raw data simulation is to physically generate the ocean data from the beginning of SAR data acquisition onboard, instead of generating the data at an output (SAR image) level. Although particularly pertaining to the ocean SAR raw data generation, Franceschetti's simulators [49], [50] show their inability to produce the VB effect. Now, a question naturally arises: How can the VB effect be physically generated via using long-wave orbital velocities as input parameters to a simulator, instead of following a posteriori way? To achieve this aim, we consider physically incorporating the ocean dynamics into the range

equation, an equation describing the instantaneous distance from the radar to a backscattering element in the illuminated scene. This strategy is shown in Fig. 2. The range equation is, as well known, the base from which the SAR raw signal is constructed [89]. With reference to Fig. 1, the range equation for a backscattering facet located at (x_m, y_n) can be expressed as (27), shown at the bottom of the page. Here, t, in terms of a SAR signal, is called the slow time referenced to the time when the antenna beam center crosses the ocean scene center, and $R_0(x_m, y_n)$ is the closest distance from the radar to the considered facet at (x_m, y_n), as given by

$$R_0(x_m, y_n) = \sqrt{\left(H - z_l^0(x_m, y_n)\right)^2 + y_n^2} \qquad (28)$$

where $z_l^0(x_m, y_n)$ is the ocean-surface height [see (5)] at coordinate (x_m, y_n) and time $t = (x_m / v - v_x^{\mathrm{cur}})$, which is expressed by

$$z_l^0(x_m, y_n) = z_l(x_m, y_n, t)|_{t = \frac{x_m}{v - v_x^{\mathrm{cur}}}}. \qquad (29)$$

5) Formulation of the Expression for the Ocean SAR Raw Data in the 2-D Time Domain: Assume that the SAR transmits pulses with a linear frequency modulation (FM), i.e., chirp modulation. Then, based on the range (27) and according to [89], the SAR raw data for the considered ocean scene shown in Fig. 1, after down conversion to baseband, can be formulated as

$$\begin{aligned}
s(\tau, t) = \sum_{m=1}^{M} \sum_{n=1}^{N} & \left[\gamma(x_m, y_n) \cdot \mathrm{rect}\left(\frac{\tau - 2r(t|x_m, y_n)/c}{T_r}\right) \right. \\
& \cdot \mathrm{rect}\left(\frac{t - x_m/(v - v_x^{\mathrm{cur}})}{T_a}\right) \\
& \times \exp\left\{-j4\pi f_0 \cdot r(t|x_m, y_n)/c\right\} \\
& \left. \cdot \exp\left\{j\pi K_r\left(\tau - 2r(t|x_m, y_n)/c\right)^2\right\} \right]
\end{aligned}$$
$$(30)$$

where τ denotes the fast time (the range time) of the SAR signal, f_0 is the radar carrier frequency, T_r is the pulse duration, K_r is the FM rate of the transmitted pulse, T_a is the SAR illumination time (the target exposure time), and $\mathrm{rect}(\cdot)$ is the standard rectangular window function, given by

$$\mathrm{rect}(t/T) = \begin{cases} 1, & \text{for } |t| \leq T/2 \\ 0, & \text{otherwise.} \end{cases} \qquad (31)$$

Now, let us make some comments on the time-domain ocean SAR raw data formula (30).

a) The VB effect does not explicitly appear in the expression for the time-domain ocean SAR raw data. Instead, the VB effect can show up in the SAR image after SAR raw data processing, which will be obvious in Section IV. This means that, for (30), the VB effect is generated through a physical way, rather than through a superimposition way at the SAR image level.

$$r(t|x_m, y_n) = \sqrt{\left[R_0(x_m, y_n) + \widehat{v}_r(x_m, y_n) \cdot \left(t - \frac{x_m}{v - v_x^{\mathrm{cur}}}\right)\right]^2 + \left[(v - v_x^{\mathrm{cur}}) \cdot t - x_m\right]^2} \qquad (27)$$

b) The randomness feature related to the spread of the radial facet velocities within one resolution cell is fully preserved in the ocean SAR raw data expression (30) since the random variable u_r [see (26)] is involved in it. Meanwhile, after raw data processing, the subresolution scale facet velocity spread can lead to a degradation in azimuth resolution, as will be shown in Section IV.

c) The expression for the time-domain ocean SAR raw data involves twofold summation and the total number of operations required for the simulation is on the order of MNL_xL_r with L_x and L_r being the sizes of the raw data in azimuth and range, respectively, meaning that the computation load for the time-domain SAR raw data simulator is *extremely high*. To improve the computational efficiency of the simulator, we must resort to frequency-domain methods, an issue to be discussed in the following.

III. IOK ALGORITHM FOR OCEAN SAR RAW DATA SIMULATION

In this section, we make an attempt to generalize the IOK algorithm [82], originally designed for the stationary land scenes, to a new version that can address the ocean scenes, with an aim of significantly reducing the computation burden associated with the time-domain ocean SAR raw data simulator shown in (30). The key issue involved in the generalization is how to handle the problem of the variation of ocean-motion parameters with space over the whole scene.

A. Recalling of the IOK Algorithm for Stationary Scenes

In preparation for the development of the new version of the IOK algorithm aimed at ocean scenes, let us first review the basic principle of the original version of this algorithm for *stationary* scenes. Because the main steps of the IOK algorithm are applied in the 2-D frequency domain, we give the expression for the SAR raw data for a stationary scene in this domain, which, according to the derivation in [89], takes the following form:

$$
\begin{aligned}
S_{\text{sta}}(f_\tau, f_d) = \sum_{m=1}^{M} \sum_{n=1}^{N} & \Big[\gamma_{\text{sta}}(x_m, R_{0_n}) \\
& \times W_r(f_\tau) \cdot W_a(f_d - f_{d_c}) \\
& \times \exp\Big\{ -j\frac{4\pi R_{0_n}}{c}\sqrt{(f_0+f_\tau)^2 - \frac{c^2 f_d^2}{4v^2}} \\
& \qquad -j\frac{\pi f_\tau^2}{K_r} - j2\pi \frac{x_m}{v} f_d \Big\} \Big]
\end{aligned} \tag{32}
$$

where the subscript "sta" means "stationary;" f_τ and f_d are the range frequency and the Doppler frequency, respectively; $W_r(f_\tau)$ denotes the spectral envelope of the transmitted chirp pulse; $W_a(f_d - f_{d_c})$ denotes the envelope of the Doppler frequency spectrum centered at the Doppler centroid frequency f_{d_c}; and $\gamma_{\text{sta}}(x_m, R_{0_n})$ is the complex reflectivity map for the considered stationary scene in the slant-range plane with R_{0_n} being the slant-range coordinate (see Fig. 1). Other symbols involved in (32), respectively, have the same meanings as those shown in (30).

The purpose of the IOK algorithm lies in generating the SAR raw data represented by $S_{\text{sta}}(f_\tau, f_d)$ while avoiding the twofold

summation shown on the right-hand side of (32) [78], [82]. According to [82], the implementation of the IOK algorithm can be expressed as

$$
\begin{aligned}
S_{\text{sta}}&(f_\tau, f_d) \\
&= \text{STO}\Big(\text{FFT}_{2D}\Big\{ \text{MAP}\left[\gamma_{\text{sta}}(x_m, R_{0_n})\right]_{x_m \to t_m \, R_{0_n} \to \tau_n} \\
& \qquad\qquad \times e^{-j2\pi f_0 \tau_n} \Big\}_{\tau_n \to \hat{f}_\tau \, t_m \to f_d} \Big)_{\hat{f}_\tau \to f_\tau} \\
& \quad \times S_{\text{sta}}^{\text{ref}}(f_\tau, f_d).
\end{aligned} \tag{33}
$$

Although the specific procedures of the IOK algorithm shown in (33) have been discussed in detail in [82], herein, for the convenience of reference in the following (Section III-B and D), we briefly repeat them as follows.

1) The starting point of the IOK algorithm is to map the coordinates (x_m, R_{0_n}) of $\gamma_{\text{sta}}(x_m, R_{0_n})$ into (t_m, τ_n), according to the following:

$$
\begin{cases}
t_m = x_m/v \\
\tau_n = 2(R_{0_n} - R_{0_c})/c
\end{cases} \tag{34}
$$

where R_{0_c} is the range of closest approach for the scene center. The aforementioned coordinate transformation can be easily realized by a linear interpolator and is represented by the operator $\text{MAP}[\cdot]$ in (33). We write the coordinate-transformed reflectivity map as $\hat{\gamma}_{\text{sta}}(\tau_n, t_m)$. Then, $\hat{\gamma}_{\text{sta}}(\tau_n, t_m)$ is multiplied by a complex factor $e^{-j2\pi f_0 \tau_n}$.

2) Afterward, a 2-D FFT is performed to transform $\hat{\gamma}_{\text{sta}}(\tau_n, t_m) \cdot e^{-j2\pi f_0 \tau_n}$ into the 2-D frequency domain, so that we obtain its 2-D Fourier transform (FT), $\Gamma_{\text{sta}}(\hat{f}_\tau, f_d)$, where $\hat{f}_\tau$ is the Fourier mate of τ_n.

3) Then, regarding $\Gamma_{\text{sta}}(\hat{f}_\tau, f_d)$, the range frequency variable $\hat{f}_\tau$ is mapped into a new range frequency variable f_τ via the following range frequency mapping function (RFMF):

$$
f_\tau = \sqrt{(f_0 + \hat{f}_\tau)^2 + \frac{c^2 f_d^2}{4v^2}} - f_0 \tag{35}
$$

so that $\Gamma_{\text{sta}}(\hat{f}_\tau, f_d)$ becomes $\hat{\Gamma}_{\text{sta}}(f_\tau, f_d)$. The above coordinate transformation, which can be achieved by a sinc interpolator [89], is called the Stolt mapping [90] and is denoted by the operator $\text{STO}(\cdot)$.

4) Once the Stolt mapping has been accomplished, a reference function multiply is performed on $\hat{\Gamma}_{\text{sta}}(f_\tau, f_d)$, so that the SAR raw data $S_{\text{sta}}(f_\tau, f_d)$ in the 2-D frequency domain can be obtained. The reference function is selected to be the 2-D spectrum of the complex SAR signal for the scene center, as given by

$$
\begin{aligned}
S_{\text{sta}}^{\text{ref}}(f_\tau, f_d) &= W_r(f_\tau) \cdot W_a(f_d - f_{d_c}) \\
& \times \exp\Big\{ -j\frac{4\pi R_{0_c}}{c}\sqrt{(f_0 + f_\tau)^2 - \frac{c^2 f_d^2}{4v^2}} \\
& \qquad -j\frac{\pi f_\tau^2}{K_r} \Big\}.
\end{aligned} \tag{36}
$$

5) A 2-D inverse FFT is performed to transform $S_{\text{sta}}(f_\tau, f_d)$ back to the time domain so that the SAR raw data in the 2-D time domain can be finally obtained.

In Appendix III, it is proved that the SAR raw data generated by the IOK algorithm shown in (33) is exactly identical to the one generated by (32). In addition, some remarks are needed to further understand the IOK algorithm.

a) With the aid of the Stolt mapping, the twofold summation on the right-hand side of (32) is replaced by a 2-D FFT, thus significantly reducing the computation complexity. Note that the number of operations needed for the IOK algorithm is on the order of $L_x L_r[1 + \log_2(L_x L_r)]$ [66], whereas that for the time-domain simulator is on the order of $MNL_x L_r$. Another purpose of the Stolt mapping is to introduce into the SAR raw data the range dependence of azimuth modulation, range cell migration, and range–azimuth coupling simultaneously and exactly.

b) The reference function multiply [see (36)] serves as two aims: The first one is to band limit the reflectivity map to generate a specific SAR resolution, and the second one is to add to the SAR raw data the range FM$\exp\{-j(\pi f_\tau^2/K_r)\}$.

B. Two-Dimensional Spectrum for Ocean-Surface Backscattering Facets

Now, let us return to the ocean SAR raw data simulation. From the recalling of the IOK algorithm for the stationary scenes, we can find that, the Stolt mapping and the reference function multiply, the two key steps of this algorithm, both require the specific form of the 2-D spectrum of the SAR signal in the range frequency and Doppler frequency domain. Therefore, in extending the original IOK algorithm to the ocean scenes, we are required to derive the 2-D spectrum of the *ocean* SAR signal according to (30). This work is left in Appendix IV. Through derivation, the 2-D spectrum for a water particle located at coordinate (x_m, y_n) in the ocean scene (see Fig. 1) can be expressed as

$$S(f_\tau, f_d) = \mathrm{rect}\left(\frac{f_\tau}{B}\right) \cdot \mathrm{rect}\left(\frac{t^* - x_m/(v - v_x^{\mathrm{cur}})}{T_a}\right) \times \exp\{j\Psi_{mn}(f_\tau, f_d)\} \tag{37}$$

where $B = K_r T_r$ is the chirp bandwidth,

$$t^* = -\frac{c\chi \cdot R_0(x_m, y_n) \cdot f_d}{2(f_0 + f_\tau)(v - v_x^{\mathrm{cur}})^2 \sqrt{1 - \frac{c^2 f_d^2}{4(v - v_x^{\mathrm{cur}})^2 (f_0 + f_\tau)^2}}} - \frac{R_0(x_m, y_n) \cdot \widehat{v}_r(x_m, y_n)}{\left[\widehat{v}_r(x_m, y_n)\right]^2 + (v - v_x^{\mathrm{cur}})^2} + x_m/(v - v_x^{\mathrm{cur}}) \tag{38}$$

and the phase of $S(f_\tau, f_d)$ is given by

$$\Psi_{mn}(f_\tau, f_d) = -\frac{4\pi\chi R_0(x_m, y_n)}{c}\sqrt{(f_0 + f_\tau)^2 - \frac{c^2 f_d^2}{4\left[\widehat{v}_r(x_m, y_n)\right]^2 + (v - v_x^{\mathrm{cur}})^2}} + 2\pi\frac{R_0(x_m, y_n) \cdot \widehat{v}_r(x_m, y_n)}{\left[\widehat{v}_r(x_m, y_n)\right]^2 + (v - v_x^{\mathrm{cur}})^2} f_d - 2\pi\frac{x_m}{v - v_x^{\mathrm{cur}}} f_d. \tag{39}$$

In (38) and (39), the factor χ is expressed as follows:

$$\chi = \sqrt{\frac{(v - v_x^{\mathrm{cur}})^2}{\left[\widehat{v}_r(x_m, y_n)\right]^2 + (v - v_x^{\mathrm{cur}})^2}}. \tag{40}$$

In order to better understand the peculiarities of the 2-D spectrum for ocean scenes in contrast to stationary scenes, we present the following remarks.

a) The 2-D spectrum shown in (37) simultaneously incorporates the information on the long-wave orbital velocities, the orbital velocity variations stemming from long wave accelerations, the short-wave velocity fluctuations within one SAR pixel, and the velocities of ocean currents. These ocean-surface motions physically enter not only the phase but also the Doppler envelop of the 2-D spectrum, a feature which is in contrast to the fact that the Doppler information related to the ocean motions is usually not available in the SAR image-based simulators.

b) As compared with the 2-D spectrum for stationary scenes, the 2-D spectrum in (37) takes on a *random* feature since the parameter $\widehat{v}_r(x_m, y_n)$ involved in this spectrum has a random component [see $u_r(x_m, y_n)$ in (26)].

c) When deriving the 2-D spectrum, Taylor expansion is not performed on the range (27), so that high-order range–azimuth coupling terms are exactly incorporated into the derived 2-D spectrum. This means that the derived 2-D spectrum is rather accurate.

With the 2-D spectrum for ocean scenes in hand, the formulation of the RFMF is in order. Following the way used to derive the RFMF for stationary scene simulation and using (39), we can derive the one used for the ocean SAR raw data simulation via the following equation:

$$-\frac{4\pi\chi R_0(x_m, y_n)}{c}\sqrt{(f_0 + f_\tau)^2 - \frac{c^2 f_d^2}{4\left[\widehat{v}_r(x_m, y_n)\right]^2 + (v - v_x^{\mathrm{cur}})^2}} + 2\pi\frac{R_0(x_m, y_n) \cdot \widehat{v}_r(x_m, y_n)}{\left[\widehat{v}_r(x_m, y_n)\right]^2 + (v - v_x^{\mathrm{cur}})^2} f_d = -\frac{4\pi R_0(x_m, y_n)}{c}(f_0 + \hat{f}_\tau). \tag{41}$$

Solving (41) for f_τ, we obtain the RFMF, given by

$$f_\tau = \sqrt{\frac{(F_0 + \hat{f}_\tau)^2}{\chi^2} + \frac{c^2 f_d^2}{4\left\{\left[\widehat{v}_r(x_m, y_n)\right]^2 + (v - v_x^{\mathrm{cur}})^2\right\}}} - f_0 \tag{42}$$

where

$$F_0 = f_0 - \frac{c \cdot \widehat{v}_r(x_m, y_n)}{2\left\{\left[\widehat{v}_r(x_m, y_n)\right]^2 + (v - v_x^{\mathrm{cur}})^2\right\}} f_d. \tag{43}$$

Unfortunately, after comparing (42) and (35), we find a problem: Due to the spatial variation of $\widehat{v}_r(x_m, y_n)$, the RFMF shown in (42) varies with the spatial coordinate (x_m, y_n), but on the other hand, the IOK algorithm requires that the RFMF
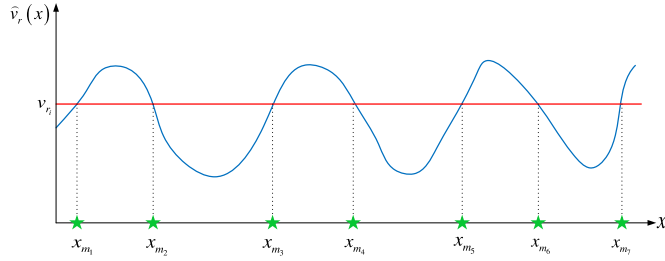
Fig. 3. Principle of batch processing. One single value of $\widehat{v}_r$ corresponds to a collection of coordinate points marked by "stars," leading to the fact that one single implementation of the IOK algorithm can simulate a group of backscattering facets.

Fig. 4. Flowchart of the proposed new version of the IOK algorithm for ocean scenes.

be independent of spatial coordinates [see (35)]. This problem makes it not straightforward to extend the original IOK algorithm to ocean scenes. In what follows, we will give a solution to this problem.

C. Use of Batch Processing to Handle the Spatial Variation of the Ocean-Motion Parameter

Typically, ocean-surface waves, particularly ocean swells with a dominant wavelength, exhibit a degree of periodicity in spatial coordinates, which makes the radial ocean-motion parameter $\widehat{v}_r(x_m, y_n)$ [see (26)] also take on a degree of periodicity, as shown in Fig. 3, where only the azimuth coordinate is considered. As shown in Fig. 3, one single value of $\widehat{v}_r$ corresponds to a collection of coordinate points (rather than one single coordinate point). Such a characteristic displayed by the ocean-motion parameter $\widehat{v}_r$ offers an opportunity to tackle the aforementioned problem when extending the original IOK algorithm to ocean scenes. In fact, just as shown in Fig. 3, *a group of* backscattering facets which have the *same* value of $\widehat{v}_r$, can be *simultaneously* simulated through one *single* implementation of the IOK algorithm. At this moment, the IOK algorithm can be implemented because the value of $\widehat{v}_r$ is fixed for these backscattering facets, so that the RFMF shown in (42) no longer varies with spatial coordinates. Then, the same procedures can be repeated for different values of $\widehat{v}_r$, so that the whole ocean scene can be simulated. Here, we call the processing strategy described above the *batch processing*, which allows us to gain partial efficiency of the original IOK algorithm, although its full computation efficiency is difficult to obtain when extending this algorithm to ocean scenes. The batch processing is the key of the new version of the IOK algorithm whose overall flowchart will be presented in what follows.

D. Flowchart of the New Version of the IOK Algorithm for Ocean Scenes

The flowchart of the main steps of the proposed new version of the IOK algorithm aimed at ocean SAR raw data simulation is exemplarily shown in Fig. 4 and explained as follows. The first level of the flowchart is relevant to prescribing the input parameters to the simulator, including the ocean wave and current parameters, the SAR system parameters, the SAR/ocean scene geometry parameters, and the electromagnetic parameters.

Afterward, the complex reflectivity map and the radial ocean-motion parameter $\widehat{v}_r(x_m, y_n)$ [see (26)] are evaluated. Details
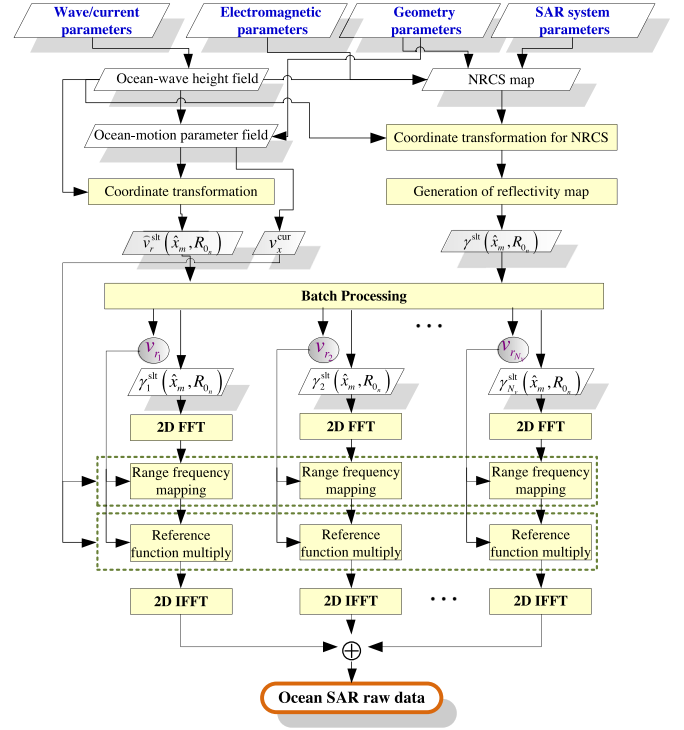
concerning the specific procedures of generating these two parameters have been given in Section II. However, some additional work needs to be done, due to the fact that these two parameters are both generated on the ground-range plane, but the IOK algorithm requires the reflectivity map to be given on the *slant* range plane [see (33)]. Therefore, we should transform the reflectivity map and the radial ocean-motion parameter $\widehat{v}_r(x_m, y_n)$ from the ground-range plane onto the slant-range plane by using the following procedures.

1) For the radial ocean-motion parameter $\widehat{v}_r(x_m, y_n)$, we map the coordinates (x_m, y_n) into $(\hat{x}_m, R_{0_n})$ via the following equation:

$$\begin{cases} \hat{x}_m = \frac{v}{v - v_x^{\mathrm{cur}}} x_m \\ R_{0_n} = R_0(x_m, y_n) \end{cases} \tag{44}$$

where $R_0(x_m, y_n)$ is shown in (28). After the coordinate mapping, $\widehat{v}_r(x_m, y_n)$ becomes $\widehat{v}_r^{\mathrm{slt}}(\hat{x}_m, R_{0_n})$, where the superscript "slt" means "slant range." Note that the coordinate mapping $x_m \to \hat{x}_m$ originates from the fact that the phase term $-2\pi(x_m/v - v_x^{\mathrm{cur}} f_d$ in (39) should be tailored to $-j2\pi(x_m/v) f_d$ in (32).

2) For the reflectivity map, we first map the NRCS of the ocean surface $\bar{\sigma}_{\mathrm{HH}}^0(x_m, y_n)$ [see (17)] from the ground-range plane onto the slant-range plane via (44), so that $\bar{\sigma}_{\mathrm{HH}}^0(x_m, y_n)$ becomes $\bar{\bar{\sigma}}_{\mathrm{HH}}^0(\hat{x}_m, R_{0_n})$. Then, based on $\bar{\bar{\sigma}}_{\mathrm{HH}}^0(\hat{x}_m, R_{0_n})$ and following the same procedures given in Section II-C [see (19)], we can get the reflectivity map expressed on the slant-range plane $\gamma^{\mathrm{slt}}(\hat{x}_m, R_{0_n})$.

Thereafter, based on the obtained $\widehat{v}_r^{\mathrm{slt}}(\hat{x}_m, R_{0_n})$ and $\gamma^{\mathrm{slt}}(\hat{x}_m, R_{0_n})$, the batch processing discussed in Section III-C

$$\delta v_r = \sqrt{E_{x,y}\left\{\left[\frac{\partial v_r^0(x_m,y_n)}{\partial x_m}\right]^2\right\} \cdot \Delta x^2 + E_{x,y}\left\{\left[\frac{\partial v_r^0(x_m,y_n)}{\partial y_n}\right]^2\right\} \cdot \Delta y^2} \tag{55}$$

(see Fig. 3) is performed. To be more specific, it consists of the following procedures.

1) Divide the velocity range $[\min_{m,n}(\widehat{v}_r^{\text{slt}}(\hat{x}_m, R_{0_n})),$ $\max_{m,n}(\widehat{v}_r^{\text{slt}}(\hat{x}_m, R_{0_n}))]$ into discrete velocity bins, so that we obtain a discrete set Θ, i.e.,

$$\Theta = \left\{v_{r_i} = \min_{m,n}\left(\widehat{v}_r^{\text{slt}}(\hat{x}_m, R_{0_n})\right) \right.$$
$$\left. + (i-1) \cdot \delta v_r|_{i=1,2,\dots,N_v}\right\} \tag{45}$$

where $\min_{m,n}(\widehat{v}_r^{\text{slt}}(\hat{x}_m, R_{0_n}))$ and $\max_{m,n}(\widehat{v}_r^{\text{slt}}(\hat{x}_m, R_{0_n}))$ are the minimum and maximum of $\widehat{v}_r^{\text{slt}}(\hat{x}_m, R_{0_n})$, respectively, δv_r is the size of one velocity bin (the interval between two adjacent values of v_{r_i}); and N_v is the dimension of the set Θ, which is linked to δv_r via

$$\delta v_r = \frac{\max_{m,n}\left(\widehat{v}_r^{\text{slt}}(\hat{x}_m, R_{0_n})\right) - \min_{m,n}\left(\widehat{v}_r^{\text{slt}}(\hat{x}_m, R_{0_n})\right)}{N_v}. \tag{46}$$

A detailed discussion of how to select the value of N_v will be left in Section III-E.

2) For a *fixed* value $v_{r_i} \in \Theta$, search the slant-range plane coordinates over the considered ocean scene to find those coordinate pairs, at which, the values of $\widehat{v}_r^{\text{slt}}(\hat{x}_m, R_{0_n})$ fall within the velocity bin $(v_{r_i} - \delta v_r/2, v_{r_i} + \delta v_r/2]$, and then group these coordinate pairs into a set Ω_i, shown as

$$\Omega_i = \left\{\left(\hat{x}_{m_1}, R_{0_{n_1}}\right)\left(\hat{x}_{m_2}, R_{0_{n_2}}, \dots\right)\right\}$$
$$= \underset{(\hat{x}_m, R_{0_n})}{\arg}$$
$$\left\{v_{r_i} - \delta v_r/2 < \hat{v}_r^{\text{slt}}(\hat{x}_m, R_{0_n}) \le v_{r_i} + \delta v_r/2\right\} \tag{47}$$

where m_1, n_1, m_2, and n_2 are all integers, with $m_1, m_2 \in \{1, 2, \dots, M\}$ and $n_1, n_2 \in \{1, 2, \dots, N\}$, and $\arg\{\cdot\}$ means taking the argument of the function $\widehat{v}_r^{\text{slt}}(\hat{x}_m, R_{0_n})$.

3) According to the coordinate set Ω_i, construct the following reflectivity map:

$$\gamma_i^{\text{slt}}(\hat{x}_m, R_{0_n}) = \begin{cases} \gamma^{\text{slt}}(\hat{x}_m, R_{0_n}), & \text{if } (\hat{x}_m, R_{0_n}) \in \Omega_i \\ 0, & \text{otherwise.} \end{cases} \tag{48}$$

4) Replace $\widehat{v}_r(x_m, y_n)$ in (42) by v_{r_i}, and we can obtain the RFMF required for the IOK algorithm, shown as

$$f_\tau = \sqrt{\frac{\left(F_{0_i} + \hat{f}_\tau\right)^2}{\chi_i^2} + \frac{c^2 f_d^2}{4\left\{v_{r_i}^2 + (v - v_x^{\text{cur}})^2\right\}}} - f_0 \tag{49}$$

where

$$F_{0_i} = f_0 - \frac{c \cdot v_{r_i}}{2\left\{v_{r_i}^2 + (v - v_x^{\text{cur}})^2\right\}} f_d \tag{50}$$

$$\chi_i = \sqrt{\frac{(v - v_x^{\text{cur}})^2}{v_{r_i}^2 + (v - v_x^{\text{cur}})^2}}. \tag{51}$$

5) Based on (37)–(39), generate the reference function required for the IOK algorithm, shown as

$$S_{\text{ref}_i}(f_\tau, f_d) = \text{rect}\left(\frac{f_\tau}{B}\right) \cdot \text{rect}\left(\frac{t_i^*(f_\tau, f_d)}{T_a}\right)$$
$$\cdot \exp\left\{j\Psi_{\text{ref}_i}(f_\tau, f_d)\right\} \tag{52}$$

where

$$t_i^*(f_\tau, f_d) = -\frac{c\chi_i \cdot R_{0_c} \cdot f_d}{2(f_0 + f_\tau)(v - v_x^{\text{cur}})^2 \sqrt{1 - \frac{c^2 f_d^2}{4(v - v_x^{\text{cur}})^2(f_0 + f_\tau)^2}}}$$
$$- \frac{R_{0_c} \cdot v_{r_i}}{v_{r_i}^2 + (v - v_x^{\text{cur}})^2} \tag{53}$$

$$\Psi_{\text{ref}_i}(f_\tau, f_d) = -\frac{4\pi\chi_i R_{0_c}}{c}\sqrt{(f_0 + f_\tau)^2 - \frac{c^2 f_d^2}{4\left[v_{r_i}^2 + (v - v_x^{\text{cur}})^2\right]}}$$
$$+ 2\pi\frac{R_{0_c} \cdot v_{r_i}}{v_{r_i}^2 + (v - v_x^{\text{cur}})^2} f_d \tag{54}$$

with $R_{0_c} = R_0(0, y_c)$ being the slant range of the closest approach to the center of the ocean scene.

6) Implement the IOK algorithm by inserting (48), (49), and (52), into (33).

7) Repeat procedures 2–6 for every v_{r_i}, $(i = 1, 2, \dots, N_v)$ within the set Θ, and finally, we can get the SAR raw data for the considered whole ocean scene.

Since the proposed new version of the IOK algorithm is aimed at ocean scenes from here, we term this new simulator shown in Fig. 4 as the IOKOS algorithm, with the last two letters "OS" meaning "ocean scenes."

E. Issue of the Selection of the Value of N_v

In the flowchart of the proposed IOKOS algorithm, there exists a parameter, i.e., N_v, that remains to be determined. Consider that, in simulating ocean SAR raw data, we divide the whole scene into discrete facets, with each facet containing a cluster of scatterers whose orbital velocities exhibit a certain extent. Therefore, the size of a velocity bin δv_r involved in (45) should be selected such that the spatial extent of those scatterers whose orbital velocities fall within a given velocity bin is commensurate with the pixel size (i.e., the facet size). To be more specific, δv_r can be computed according to (55), shown at the top of the page, where $E_{x,y}\{[(\partial v_r^0(x_m, y_n/\partial x_m)]^2\}$ and $E_{x,y}\{[(\partial v_r^0(x_m, y_n)/\partial y_n)]^2\}$ are the mean square slopes

$$\delta v_r = \frac{1}{\sqrt{2}\xi_0}\sqrt{\iint E_l(k_x,k_y)\omega_{k_x,k_y}^2 g_{k_x,k_y}^2 \cdot \left(k_x^2 \Delta x^2 + k_y^2 \Delta y^2\right) dk_x dk_y} \tag{56}$$

$$N_v = \left\lceil \frac{\max\limits_{m,n}\left(\hat{v}_r^{\text{slt}}\left(\hat{x}_m, R_{0_n}\right)\right) - \min\limits_{m,n}\left(\hat{v}_r^{\text{slt}}\left(\hat{x}_m, R_{0_n}\right)\right)}{\sqrt{\iint E_l(k_x,k_y)\omega_{k_x,k_y}^2 g_{k_x,k_y}^2 \cdot \left(k_x^2 \Delta x^2 + k_y^2 \Delta y^2\right) dk_x dk_y}/\sqrt{2}\xi_0} \right\rceil \tag{57}$$

of $v_r^0(x_m, y_n)$ in directions of x_m and y_n, respectively, with $E_{x,y}\{\cdot\}$ denoting the 2-D expectation operator, and $v_r^0(x_m, y_n)$ is shown in (21). The physical meaning of (55) is that the velocity-bin size δv_r involved in (45) is set equal to the rms orbital-velocity extent of the scatterers within one facet. Alternatively, we can also express δv_r in terms of the long ocean wave spectrum (i.e., the JONSWAP spectrum). Based on (7), (12), and (21), and using the assumption that all components of the long ocean wave spectrum are independent of each other, we can, after some simple manipulations, further express (55) as (56), shown at the top of the page, where $E_l(k_x, k_y)$ is the JONSWAP spectrum shown in (59). Then, according to (46) and (56), N_v can be evaluated as (57), shown at the top of the page, where the operator $\lceil \cdot \rceil$ denotes rounding its argument to the nearest integer. The validity of (57) will be demonstrated using simulation results in Section IV-A.3.

F. Computation Load

Now, let us compare the computation complexity for the original version of the IOK algorithm shown in (33), the newly proposed IOKOS algorithm shown in Fig. 4, and the time-domain simulator shown in (30). As discussed earlier, the number of the operations required for the original version of the IOK algorithm is on the order of $L_x L_r[1 + \log_2(L_x L_r)]$. For the IOKOS algorithm, the procedures involved in (33) are repeated N_v times, as shown in Fig. 4; therefore, the computation complexity for the IOKOS algorithm is on the order of $N_v L_x L_r[1 + \log_2(L_x L_r)]$. By contrast, the computation complexity for the time-domain simulator shown in (30) is on the order of $MNL_x L_r$. To consider an example, let us suppose that the considered ocean scene consists of $M \times N = 1024 \times 1024$ backscattering facets, the SAR raw data has $L_x \times L_r = 1024 \times 1024$ pixels, and N_v equals 50. Then, the computation complexity values for the time-domain simulator, the original IOK algorithm, and the IOKOS algorithm are 1099.5×10^9, 0.022×10^9, and 1.1×10^9 operations, respectively. It is found that, although slower than the original IOK algorithm, the IOKOS algorithm is *much faster* than the time-domain simulator. Note that the efficiency of the IOKOS algorithm is nearly 10^3 times *higher* than that of the time-domain simulator.

IV. SIMULATION RESULTS

Here, simulation results are provided, aimed at evaluating the performance of the IOKOS algorithm developed in Section III.

TABLE I
INPUT PARAMETERS TO THE IOKOS SIMULATOR

Parameter	Value	
PRF	3040 Hz	
Radar carrier frequency	9.6 GHz	
Pulse duration	50 μs	
Range sampling rate of radar	80 MHz	
Chirp bandwidth	40 MHz	
Doppler bandwidth	1520 Hz	
Antenna length in azimuth	10 m	
Radar platform velocity	7600 m/s	
Radar platform altitude	700 km	
Incidence angle at scene center	45.0^o	
Scene dimension (azimuth × ground range)	5.12 km × 5.43 km	
Azimuth resolution	5.0 m	
Ground range resolution	5.3 m	
Phillips parameter of the short-wave spectrum	0.0081	
Relative dielectric constant of ocean water	$48 - 35j$	
SAR raw data sizes ($L_x \times L_r$)	2048 × 2048	
Velocity component of current in azimuth	0.6 m/s	
Velocity component of current in ground range	0.7 m/s	
Two cases of ocean swells	Case I (Narrow band)	Case II (Broad band)
Wind speed at a height of 19.5 m	4 m/s	16 m/s
Width of JONSWAP spectrum (σ_a, σ_b)	0.02, 0.02	0.15, 0.15
Peak enhancement factor of JONSWAP spectrum	20	5
Significant wave height	4 m	4 m
Wavelength of the dominant long wave	200 m	200 m
Direction of the dominant long wave	45.0^o	45.0^o
Dimension of Θ (N_v)	117	143

The required simulation parameters are summarized in Table I. Here, we consider a spaceborne SAR system with HH polarization and two ocean scenes featuring ocean swells and a constant current. For the first ocean scene (Case I), the swell spectrum is relatively narrow, whereas for the second one (Case II), the swell spectrum is relatively broad. The SAR raw data for the considered ocean scenes were simulated using the procedures shown in Fig. 4. The oversampling ratio in azimuth and that in
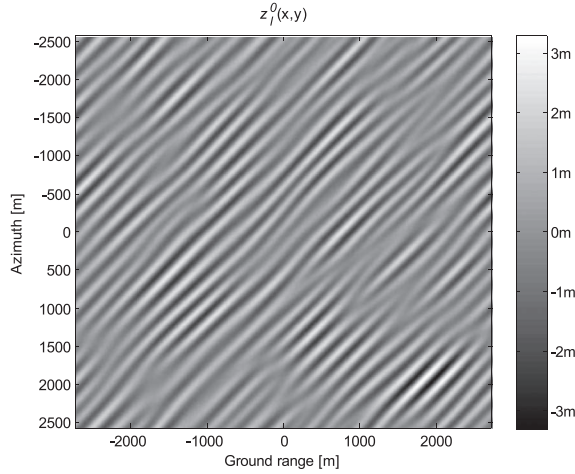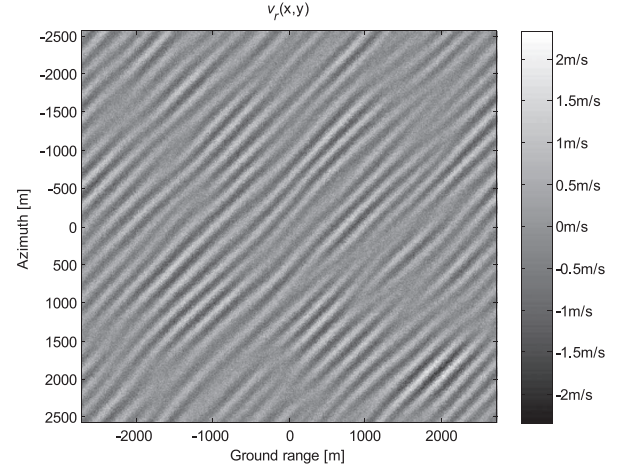
Fig. 5. Ocean-surface height field for Case I.

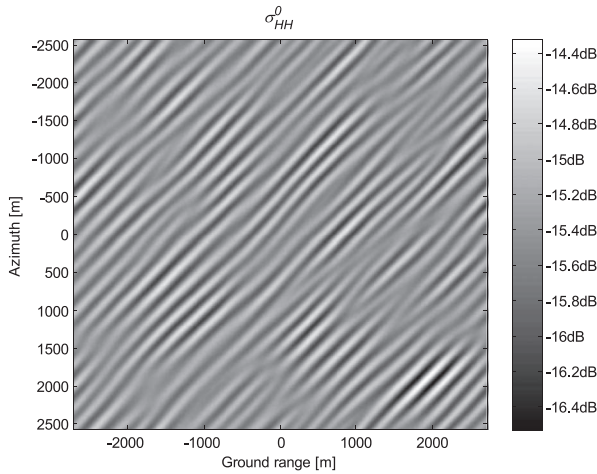Fig. 6. Evaluated NRCS map for Case I.

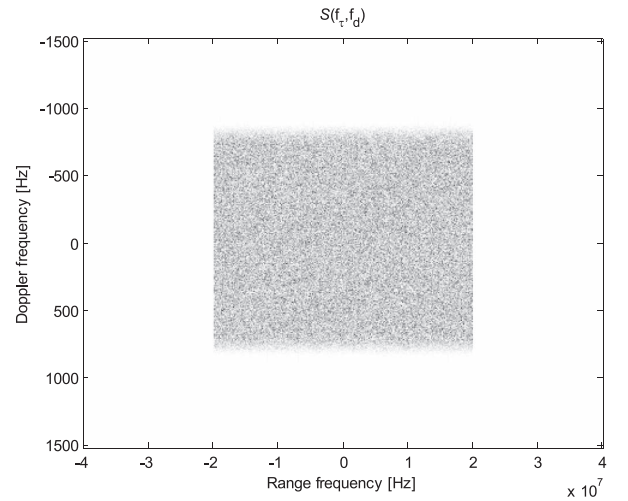Fig. 7. Ocean-surface radial velocity field for Case I.

Fig. 8. Two-dimensional spectrum of the simulated SAR raw data for Case I.

range were both set to be 2, so that one resolution cell contains four backscattering facets (i.e., four SAR pixels).[4]

A. Case I: Narrow-Band Swell Spectrum

For Case I (narrow-band swell), simulation results after implementing some representative steps of the IOKOS algorithm (see Fig. 4) are, respectively, given as follows.

- The 2-D ocean-surface height field, which was generated according to (29), is shown in Fig. 5, from which we can evidently see wave patterns.
- The 2-D NRCS map corresponding to Fig. 5, which was evaluated by using (17), is presented in Fig. 6. Note that the wave-like patterns in this figure originates from the tilt modulation and the hydrodynamic modulation.
- The 2-D ocean-surface radial velocity field, evaluated by using (26), is given in Fig. 7, from which we can observe a noisy feature. Note that the noise exhibited in Fig. 7 corresponds to the random distribution of radial facet velocities associated with short waves, which is modeled in this paper as the vibration of water particles, as shown in Fig. 2.

- The gray-level representation of the simulated SAR raw data in the 2-D frequency domain for the considered ocean scene (Case I) is shown in Fig. 8, from which we can see its range frequency envelope and Doppler envelope.
- Fig. 9(a) shows the corresponding SAR image obtained from processing the resultant SAR raw data, using the Omega-K algorithm [89] with a static scene parameter setting. By comparing Figs. 5 and 9(a), we can see that the wave patterns are adequately reflected in the SAR image.
- In order to visually highlight the batch processing strategy proposed in Section III-C, we also simulated the SAR raw data corresponding to only one single value of v_{r_i} [see (45)]. The corresponding SAR image is shown in Fig. 10. As shown in Fig. 10, one single implementation of the IOK algorithm [82] can simultaneously simulate a collection of backscattering facets that have the same radial velocity, thus allowing the efficiency of the IOK algorithm to be partially gained.

In order to further assess the validity of the proposed IOKOS algorithm, we shall discuss the resultant SAR raw data from the following five aspects.

1) Wavelength and Direction of the Dominant Wave: First, let us examine the wavelength and the propagation direction

---

[4]The oversampling ratio is defined as the ratio of the sampling rate to the signal bandwidth and also equivalently defined as the ratio of the resolution to the sampling spacing (i.e., the size of one SAR pixel) [89].
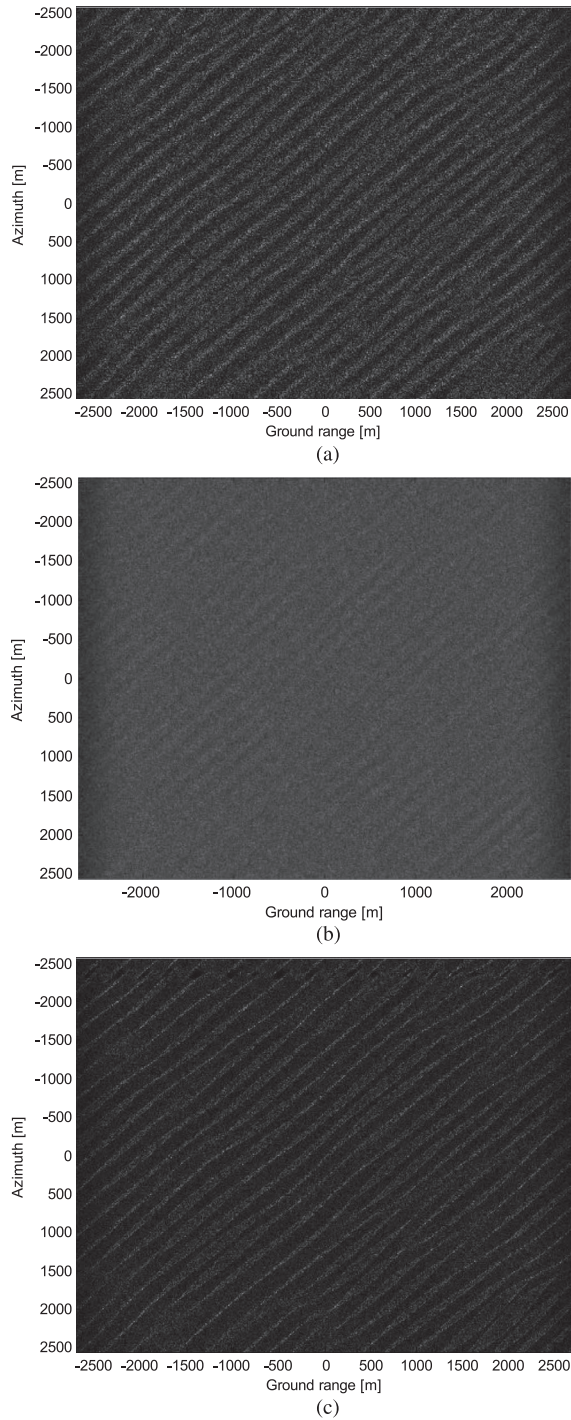
(a)

(b)

(c)

Fig. 9. SAR images from processing the resultant SAR raw data simulated with the IOKOS algorithm for Case I. (a) SAR image with all imaging mechnisms taken into account. (b) SAR image when $v_r^0(x_m, y_n)$ is set equal to zero. (c) SAR image when $u_r(x_m, y_n)$ is set equal to zero.

of the dominant wave of the considered ocean scene (Case I). To this end, we have transformed the SAR intensity image shown in Fig. 9(a) into its 2-D wavenumber domain, so that the corresponding SAR image spectrum[5] can be obtained, as shown
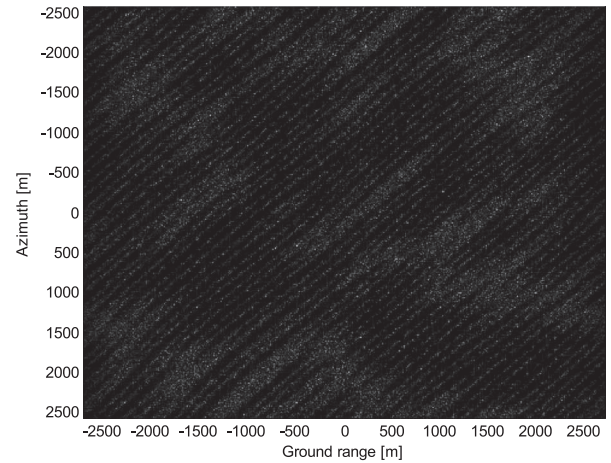

Fig. 10. SAR image from the SAR raw data simulated via one single implementation of the IOK algorithm with $v_{r_i} = 0.1289$ m/s.
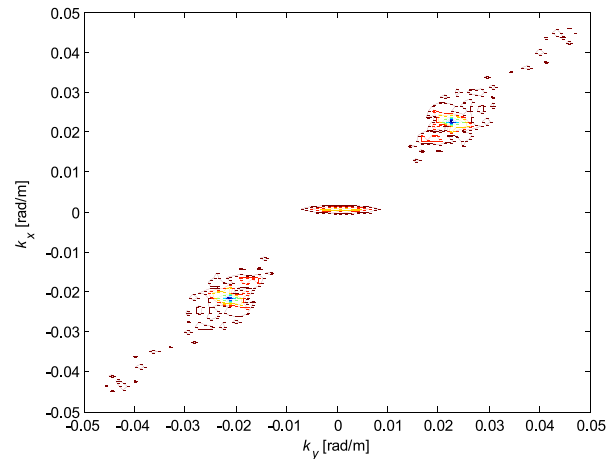

Fig. 11. SAR image spectrum obtained from Fourier transforming the SAR image shown in Fig. 9(a).

in Fig. 11. The peak wavenumber vector of the image spectrum were measured from Fig. 11 to be 0.0226 rad/m in azimuth and 0.0227 rad/m in ground range, on the basis of which, the wavelength and the direction of the dominant wave were evaluated to be 196.2 and 45.1°, respectively. On the other hand, the actual wavelength and direction of the dominant wave are 200 m and 45°, respectively, meaning that the dominant wave of the ocean scene is properly incorporated into the SAR raw data.

2) Velocity Bunching Effect: In order to check whether the VB effect is adequately reflected in the SAR image, we have set the long-wave orbital radial velocity field $v_r^0(x_m, y_n)$ in (26) equal to zero and then resimulated the raw data. After processing the resultant raw data, we have obtained the corresponding SAR image, which is shown in Fig. 9(b). Comparison of Fig. 9(a) and (b) shows that the long-wave orbital radial velocities play a remarkable role in generating the wave-like patterns [when $v_r^0(x_m, y_n)$ is set equal to zero, the wave-like patterns are significantly weakened], meaning that the VB effect is successfully embodied in the SAR image. Here, it should be emphasized that the VB effect is physically generated via using long-wave orbital velocities as input parameters to the simulator, instead of at the image level as done in most of SAR image-based simulators [4], [7], [11]–[14], [23], [44], [48].

---

[5]Note that the difference between the 2-D frequency spectrum of the SAR raw data (see Fig. 8) and the SAR image spectrum (see Fig. 11): The 2-D frequency spectrum is obtained by performing the 2-D FT on the complex SAR raw data, whereas the SAR image spectrum is obtained by performing the 2-D FT on the modulus of the SAR image.
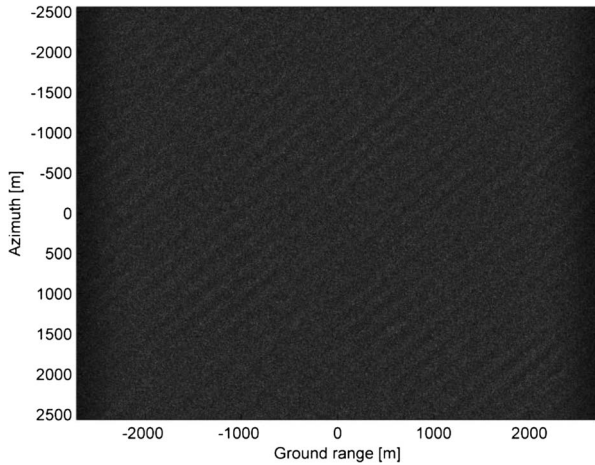
Fig. 12. SAR image by Franceschetti's simulator [49].

Fig. 13. Histogram of the normalized SAR image shown in Fig. 9(a) with the superimposition of the pdf of the K distribution.

Fig. 14. Curve of the variation of K-distribution shape parameter ν with N_v.

Also note that the benchmark ocean SAR raw data simulators, i.e., Franceschetti's simulators [49], [50], do not consider the VB effect, although they incorporate the long-wave phase velocity and the nonlinear hydrodynamic interactions between ocean waves [49]. To visualize this fact, we have also simulated another set of SAR raw data using Franceschetti's simulator [49] based on the same parameters as those used for the IOKOS simulator. The corresponding SAR image related to Franceschetti's simulator is shown in Fig. 12. It is found that the SAR image in Fig. 12 is quite similar to that in Fig. 9(b), but evidently different from that in Fig. 9(a), which clearly exhibits the VB effect, meaning that Franceschett's simulator has a limitation in embodying the VB effect.[6]

3) Statistical Features: We can also appreciate the simulated SAR raw data from the statistical perspective. To do so, the modulus of the SAR image shown in Fig. 9(a) was first normalized to its rms value so that the second moment of the image modulus evaluates to one. Then, we estimated the histogram of the normalized SAR image modulus, which is presented in Fig. 13. As is well known, the K distribution is rather appropriate to characterize the statistical features of high-resolution radar imagery of the ocean [98], [99]. Now let us examine whether the normalized SAR image modulus follows the K distribution. The two parameters involved in the K distribution, i.e., the scale parameter b and the shape parameter ν were estimated by solving the following system of equations:

$$\begin{cases} \langle I^2 \rangle = b^{-1} \dfrac{\Gamma(\nu+1)}{\Gamma(\nu)} \\ \langle I^3 \rangle = b^{-1.5} \dfrac{\Gamma(2.5)\Gamma(\nu+1.5)}{\Gamma(\nu)} \end{cases} \tag{58}$$

where I denotes the SAR image modulus, and $\langle I^2 \rangle$ and $\langle I^3 \rangle$ are the second and third moments of I, respectively. Based

[6]The computational complexity of Franceschetti's simulator [49], of course, is lower than that of the proposed IOKOS simulator. In fact, Franceschetti's simulator in [49] relies on a SAR raw data simulator called the SARAS simulator [53], whose computational complexity, according to [82], is comparable with that of the original version of the IOK algorithm [82]. According to our discussion in Section III-F, the original version of the IOK algorithm is N_v times faster than the proposed IOKOS simulator. Therefore, Franceschetti's simulator [49] is approximately N_v times faster than the proposed IOKOS simulator. It should be noted, however, that the higher efficiency of Franceschetti's simulator is achieved at the cost of its inability to embody the VB effect (see Fig. 12).
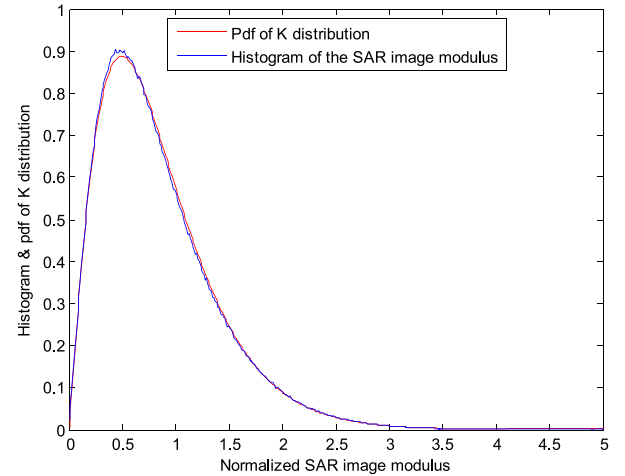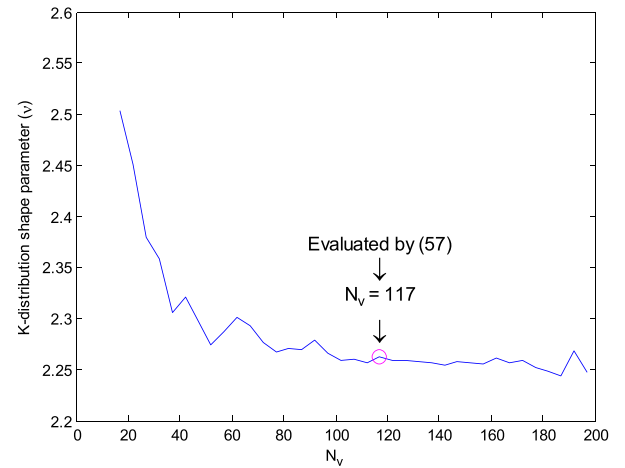
on (58), the values of b and ν for the considered SAR image were estimated to be 2.26 and 2.26, respectively. Then, the K-distribution probability density function (pdf) with $b = 2.26$ and $\nu = 2.26$ substituted into it, is plotted and superimposed on the histogram of I, as shown in Fig. 13, from which, a perfect data fit of the theoretical K-distribution model can be found. This means that the proposed IOKOS algorithm does a good job in embodying the statistical characteristics of the ocean.

The statistical feature of a SAR image can also be exploited to validate the rule for determining the value of N_v [i.e., (57)]. To this end, we simulated several raw-data sets based on different values of N_v, processed them, and then computed the respective values of the K-distribution shape parameter ν of the resulting SAR images. Fig. 14 plots the curve of the variation of K-distribution shape parameter ν with N_v. As shown in Fig. 14, when N_v exceeds the value that is computed via (57), the K-distribution shape parameter ν approximately tends to converge. In other words, if too small a value of N_v is selected [i.e., much smaller than the value computed via (57)], then the SAR image fidelity (accuracy) will suffer due to a poor velocity resolution, whereas if too large a value of N_v is selected, then unnecessary computations will be performed. This demonstrates the validity of the rule for determining the value of N_v via (57).
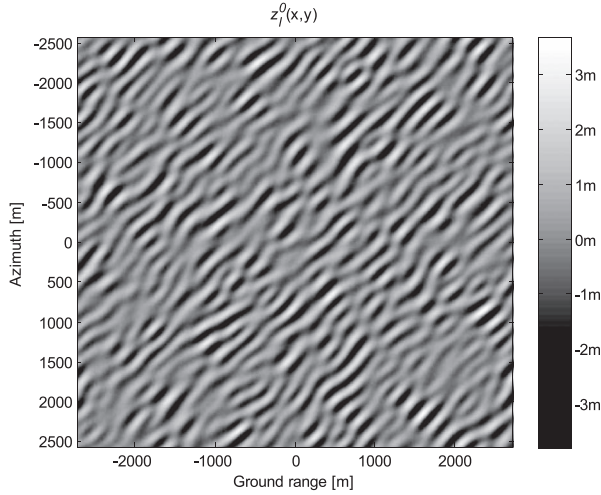
Fig. 15. Two-dimensional ocean-surface height field for Case II (broadband swell spectrum).

4) Wave Velocity Spread Within One Resolution Cell: In order to emphasize the effect of the spread of radial facet velocities within one resolution on SAR imaging, we have set $u_r(x_m, y_n)$ in (26) (see also Fig. 2) equal to zero and then resimulated the raw data. After processing the resultant raw data, we have obtained the corresponding SAR image, which is shown in Fig. 9(c). After comparing Fig. 9(a) and (c), we find that the presence of the spread of radial facet velocities *smears* the SAR image, thus leading to a degradation in azimuth resolution. Furthermore, we have also estimated the shape parameter ν of the K distribution for the SAR image shown in Fig. 9(c), and this value is 1.14. By contrast, the value of ν for the SAR image shown in Fig. 9(a) was estimated to be 2.26, meaning that the spread of radial facet velocities also influences the statistical feature of the SAR image. In fact, as is evident in Fig. 9(a) and (c), the SAR image becomes more homogeneous when the spread of radial facet velocities is introduced into the SAR raw data.

5) Doppler Centroid: Now, we shall examine whether the ocean current specified in Table I is properly incorporated in the simulated SAR raw data. Here, we adopt the SAR-signal Doppler centroid as the indicator of the current since the radial component of the current velocity vector is proportionally linked to the Doppler centroid. By utilizing the average cross-correlation coefficient method proposed in [100], the Doppler centroid of the simulated complex raw data shown in Fig. 8 was estimated to be 32.55 Hz, whereas the actual Doppler centroid computed according to the actual value of the current velocity vector is 31.68 Hz. Note that the relative difference between the actual Doppler centroid and the measured one is 2.77%, a value low enough to indicate that the proposed IOKOS algorithm performs quite well in embodying ocean currents. This is attributed to the fact that in deriving the RFMF, no Taylor expansion is made on the range equation.

B. Case II: Broad-Band Swell Spectrum

In order to demonstrate the ability of the proposed IOKOS algorithm to address broadband ocean swells, we have simulated another raw data set based on the swell parameters specified for
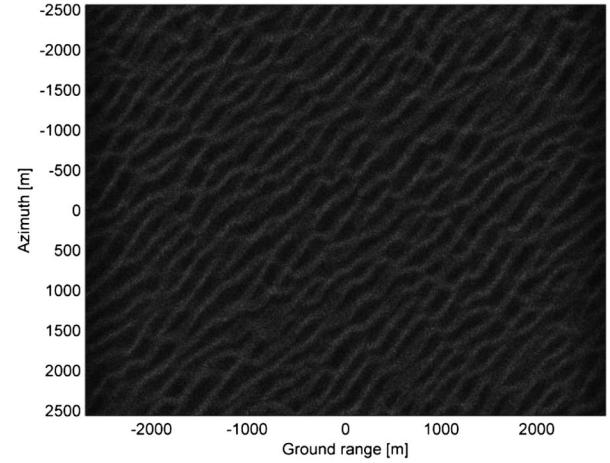

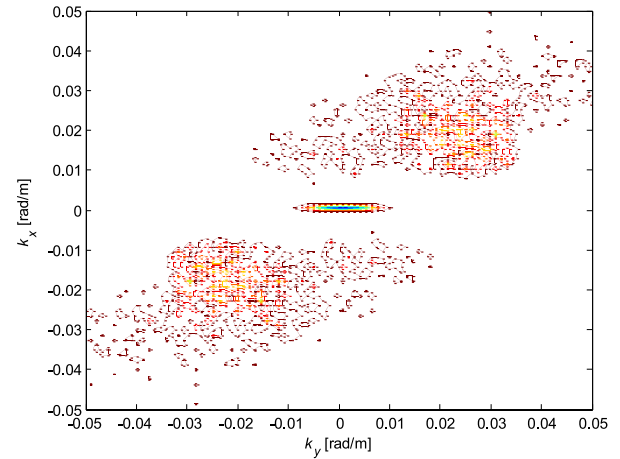Fig. 16. SAR image by the IOKOS algorithm for Case II.

Fig. 17. SAR image spectrum corresponding to the SAR image shown in Fig. 16.

Case II (the broadband swell case) shown in Table I. Fig. 15 shows the generated 2-D ocean-surface height field for this case, whereas Fig. 16 shows the SAR image resulting from processing the simulated raw data. The SAR image spectrum corresponding to the SAR image in Fig. 16 is shown in Fig. 17. A comparison of Figs. 9(a) and 16 demonstrates that there are more swell components for Case II than for Case I. Furthermore, the broadband characteristic of the SAR image in Fig. 16 can also be seen through the comparison of Figs. 11 and 17.

Before finishing our discussion, we shall make an examination on the relationship between the parameter N_v and the bandwidth of a wave spectrum. According to (57), the values of N_v for Case I (narrow-band case) and Case II (broad-band case) were evaluated to be 117 and 143, respectively, which means that the larger the bandwidth of a wave spectrum (i.e., the greater the complexity of a wave field), the higher value N_v will take.

V. CONCLUSION

In this paper, we have generalized the IOK algorithm [82], which was originally designed for the stationary land scenes, to a new version that can address the ocean scenes featuring ocean-surface waves and currents, so that a new simulator

called the IOKOS algorithm has been developed. The generalization consists of two manipulations. First, specially aimed at ocean dynamics of ocean waves and currents, the 2-D spectrum of the SAR signal was derived. Second, to account for the spatial variation of ocean-motion parameters, we adopted a strategy called batch processing, whose basic feature is that, a single implementation of the IOK algorithm will simultaneously simulate a collection of ocean-surface backscattering elements that have the same radial velocity. The proposed IOKOS algorithm can be regarded as a 3-D version of the IOK algorithm, because, apart from the range frequency and the Doppler frequency, an additional dimension, i.e., the radial velocity [see (45)] is added to the IOK algorithm [see (49) and (52)]. Although slower than the original IOK algorithm, the IOKOS algorithm is still much faster than its time-domain counterpart developed in Section II.

For the proposed IOKOS algorithm, the VB effect is embodied via making the long-wave radial orbital velocities physically enter the range equation of the SAR raw signal, instead of superimposing this effect onto the reflectivity map. Note that the ability of the IOKOS algorithm to reflect the VB effect is a characteristic that other ocean SAR raw data simulators, e.g., Franceschetti's simulators [49], [50], do not share. In order to account for the random spread of the facet velocities within one resolution cell, we adopted a means of a random *perturbation* of the local long-wave orbital velocity, in contrast to the conventional way adopted by many image-based simulators in which the spread of the radial facet velocities was made equivalent to a degradation in the azimuth resolution.

To assess the performance of the IOKOS algorithm, we have performed simulations and discussed the simulation results from five aspects: the wavelength and direction of the dominant wave, the VB effect, statistical features of the resulting SAR imagery, the wave velocity spread within one resolution cell, and the Doppler centroid. The simulation results show that the proposed IOKOS algorithm performed quite well in all these five aspects. Furthermore, the simulation results also demonstrate the ability of our simulator to address ocean swells with broadband spectra.

APPENDIX I
EXPRESSION FOR THE JONSWAP SPECTRUM

According to [44] and [95], the specific expression for the JONSWAP spectrum can be expressed as

$$E_l(k_x, k_y)$$

$$= \frac{\alpha}{2} \left[k_x^2 + k_y^2 \right]^{-2} \times \exp\left\{ -\frac{5}{4} \left[\sqrt{k_x^2 + k_y^2}/k_p \right]^{-2} \right.$$

$$+ \ln(\mu) \cdot \exp\left[-\left(\sqrt{\left(k_x^2 + k_y^2 \right)^{1/2}} - \sqrt{k_p} \right)^2 / \left(2\sigma_J^2 k_p \right) \right] \right\}$$

$$\times \frac{1}{\sqrt{\pi}} \frac{\Gamma(1 + p/2)}{\Gamma(0.5 + p/2)} \cdot \cos^{2p}\left(\mathrm{atan}\left(\frac{k_y}{k_x} \right) - \phi_p \right) \quad (59)$$

where α is the Phillips parameter describing the intensity of the wave spectrum; k_p is the peak wavenumber of the JONSWAP spectrum; ϕ_p is the angle between the wave propagation direction of the dominant wave and the along-track direction,

as shown in Fig. 1; μ is the peak enhancement factor; the parameter σ_J assumes the following expression:

$$\sigma_J = \begin{cases} \sigma_a, & \sqrt{k_x^2 + k_y^2} \le k_p \\ \sigma_b, & \sqrt{k_x^2 + k_y^2} > k_p \end{cases} \quad (60)$$

with σ_a and σ_b being two parameters characterizing the width of the JONSWAP spectrum; and the factor p in the spreading function $\cos^{2p}(\mathrm{atan}(k_y/k_x) - \phi_p)$ takes the following form:

$$p = \begin{cases} 5.29 \cdot \left(\sqrt{k_x^2 + k_y^2}/k_p \right)^{-1.25} \cdot \left(U/\sqrt{g/k_p} \right)^{-2.5}, & \sqrt{k_x^2 + k_y^2} \ge k_p \\ 5.29 \cdot \left(\sqrt{k_x^2 + k_y^2}/k_p \right)^{2.5} \cdot \left(U/\sqrt{g/k_p} \right)^{-2.5}, & \sqrt{k_x^2 + k_y^2} < k_p \end{cases} \quad (61)$$

with U denoting the wind speed at a height of 19.5 m. In (59), $\Gamma(\cdot)$ is the gamma function.

APPENDIX II
EXPRESSION FOR $\sigma_{HH_{\mathrm{tilt}}}^0(x_m, y_n, t)$

According to [11], $\sigma_{HH_{\mathrm{tilt}}}^0(x_m, y_n, t)$ can be expressed as

$$\sigma_{HH_{\mathrm{tilt}}}^0(x_m, y_n, t) = 4\pi k^4 \cos^4(\hat{\theta})$$

$$\times \left| \left(\frac{\sin(\theta + \delta_y(t)) \cos(\delta_x(t))}{\sin(\hat{\theta})} \right)^2 g_{\mathrm{VV}}(\hat{\theta}) \right.$$

$$\left. + \left(\frac{\sin(\delta_x(t))}{\sin(\hat{\theta})} \right)^2 g_{\mathrm{HH}}(\hat{\theta}) \right|^2$$

$$\times E_s(2k \sin(\theta + \delta_y(t)),$$
$$2k \cos(\theta + \delta_y(t)) \sin(\delta_x(t))) \quad (62)$$

where k is the wavenumber of the incident electromagnetic wave; θ is the incidence angle which is a function of the ground-range coordinate of the ocean scene (see Fig. 1), as given by

$$\theta(y_n) = \mathrm{atan}\left(\frac{y_n}{H} \right) \quad (63)$$

δ_x and δ_y are, respectively, expressed as

$$\delta_x = \mathrm{atan}\left(\frac{\partial z_l(x_m, y_n, t)}{\partial x_m} \right) \quad (64)$$

$$\delta_y = \mathrm{atan}\left(\frac{\partial z(x_m, y_n, t)}{\partial y_n} \right) \quad (65)$$

and $E_s(\cdot, \cdot)$ is shown in (9). In (62), $g_{\mathrm{HH}}(\hat{\theta})$ and $g_{\mathrm{VV}}(\hat{\theta})$ are respectively given as follows:

$$g_{\mathrm{HH}}(\hat{\theta}) = \frac{\varepsilon - 1}{\left[\cos(\hat{\theta}) + \left(\varepsilon - \sin^2(\hat{\theta}) \right)^{1/2} \right]^2} \quad (66)$$

$$g_{\mathrm{VV}}(\hat{\theta}) = \frac{(\varepsilon - 1)\left[\varepsilon\left(1 + \sin^2(\hat{\theta}) \right) - \sin^2(\hat{\theta}) \right]}{\left[\varepsilon \cos(\hat{\theta}) + \left(\varepsilon - \sin^2(\hat{\theta}) \right)^{1/2} \right]^2} \quad (67)$$

where ε is the relative dielectric constant of ocean water, and $\hat{\theta}$ is given by

$$\hat{\theta} = \mathrm{acos}\left[\cos(\delta_x) \cos(\theta + \delta_y) \right]. \quad (68)$$

APPENDIX III
PROOF OF THE EQUIVALENCE BETWEEN (32) AND (33)

Since $\Gamma_{\text{sta}}(\hat{f}_\tau, f_d)$ is the 2-D FT of $\hat{\gamma}_{\text{sta}}(\tau_n, t_m) \cdot e^{-j2\pi f_0 \tau_n}$, $\Gamma_{\text{sta}}(\hat{f}_\tau, f_d)$ can be expressed as

$$\Gamma_{\text{sta}}(\hat{f}_\tau, f_d) = \sum_{m=1}^{M} \sum_{n=1}^{N} [\hat{\gamma}_{\text{sta}}(\tau_n, t_m)$$
$$\cdot \exp\left\{ -j2\pi\hat{f}_\tau \cdot \tau_n - j2\pi f_d \cdot t_m - j2\pi f_0 \cdot \tau_n \right\}]. \quad (69)$$

Substituting (35) into (69) yields the following:

$$\hat{\Gamma}_{\text{sta}}(f_\tau, f_d) = \Gamma_{\text{sta}}(\hat{f}_\tau, f_d)\Big|_{\hat{f}_\tau = \sqrt{(f_0 + f_\tau)^2 - \frac{c^2 f_d^2}{4v^2}} - f_0}$$

$$= \sum_{m=1}^{M} \sum_{n=1}^{N} \left[\hat{\gamma}_{\text{sta}}(\tau_n, t_m) \cdot \right.$$
$$\times \exp\left\{ -j2\pi\sqrt{(f_0 + f_\tau)^2 - \frac{c^2 f_d^2}{4v^2}} \right.$$
$$\left. \left. \cdot \tau_n - j2\pi f_d \cdot t_m \right\} \right]. \quad (70)$$

Then, multiplying (70) with $S_{\text{sta}}^{\text{ref}}(f_\tau, f_d)$ [see (36)], we have

$$\hat{\Gamma}_{\text{sta}}(f_\tau, f_d) \cdot S_{\text{sta}}^{\text{ref}}(f_\tau, f_d)$$
$$= \sum_{m=1}^{M} \sum_{n=1}^{N} [\hat{\gamma}_{\text{sta}}(\tau_n, t_m) \cdot W_r(f_\tau) \cdot W_a(f_d - f_{d_c})$$
$$\times \exp\left\{ -j2\pi\sqrt{(f_0 + f_\tau)^2 - \frac{c^2 f_d^2}{4v^2}} \cdot \tau_n \right.$$
$$\left. -j\frac{4\pi R_{0_c}}{c}\sqrt{(f_0 + f_\tau)^2 - \frac{c^2 f_d^2}{4v^2}} - j\frac{\pi f_\tau^2}{K_r} - j2\pi f_d \cdot t_m \right\}]. \quad (71)$$

By inserting (34) into (71), we find that $\hat{\Gamma}_{\text{sta}}(f_\tau, f_d) \cdot S_{\text{sta}}^{\text{ref}}(f_\tau, f_d)$ is exactly equal to the right-hand side of (32), meaning that (32) and (33) are equivalent to each other.

APPENDIX IV
DERIVATION OF THE 2-D SPECTRUM OF THE OCEAN SAR SIGNAL

Here, we will derive the closed-form expression for the 2-D spectrum of the complex SAR signal for ocean scenes featuring waves and currents. Let us consider a water particle located at coordinate (x_m, y_n) in the ocean scene (see Fig. 1). Based on (30) and according to [89], the 2-D spectrum for this water particle, ignoring its reflectivity, can be expressed as

$$S(f_\tau, f_d) = \text{rect}\left(\frac{f_\tau}{B}\right) \cdot \int_{-\infty}^{\infty} \text{rect}$$
$$\left(\frac{t - x_m/(v - v_x^{\text{cur}})}{T_a}\right) \exp\left\{ j\psi(t) \right\} dt \quad (72)$$

where $B = K_r T_r$ is the chirp bandwidth and

$$\psi(t) = -\frac{4\pi(f_0 + f_\tau)r(t|x_m, y_n)}{c} - \frac{\pi f_\tau^2}{K_r} - 2\pi f_d t \quad (73)$$

with $r(t|x_m, y_n)$ shown in (27). Solving

$$\frac{d\psi(t)}{dt}\Big|_{t=t^*} = 0 \quad (74)$$

we can obtain the stationary phase point t^*, which is shown in (38). Applying the POSP [89] to (72), we can get the closed-form expression for $S(f_\tau, f_d)$, given by

$$S(f_\tau, f_d) = \text{rect}\left(\frac{f_\tau}{B}\right) \cdot \text{rect}$$
$$\left(\frac{t^* - x_m/(v - v_x^{\text{cur}})}{T_a}\right) \cdot \exp\left\{ j\psi(t^*) \right\}. \quad (75)$$

After some tedious but trivial manipulations, we finally have (37)–(40).

REFERENCES

[1] R. O. Harger, *Synthetic Aperture Radar System: Theory and Design.* New York, NY, USA: Academic, 1970.
[2] S. Martin, *An Introduction To Ocean Remote Sensing.* Cambridge, U.K.: Cambridge Univ. Press, 2014.
[3] M. K. Hsu and A. K. Liu, "Nonlinear internal waves in the South China Sea," *Can. J. Remote Sens.*, vol. 26, no. 2, pp. 72–81, 2000.
[4] C. L. Rufenach and W. A. Alpers, "Imaging ocean waves by synthetic aperture radars with long integration times," *IEEE Trans. Antennas Propag.*, vol. AP-29, no. 3, pp. 422–428, May 1981.
[5] P. M. DiGiacomo and B. Holt, "Satellite observations of small coastal eddies in the Southern California Bight," *J. Geophys. Res.*, vol. 106, no. C10, pp. 22 521–22 543, Oct. 2001.
[6] L. Shemer, M. Marom, and D. Markan, "Estimates of currents in the nearshore ocean region using interferometric synthetic aperture radar," *J. Geophys. Res.*, vol. 98, no. C4, pp. 7001–7010, Apr. 1993.
[7] W. R. Alpers and C. L. Rufenach, "The effect of orbital motions on synthetic aperture radar imaging of ocean waves," *IEEE Trans. Antennas Propag.*, vol. AP-27, no. 5, pp. 685–690, Sep. 1979.
[8] M. J. Rouault, A. Mouche, F. Collard, J. A. Johannessen, and B. Chapron, "Mapping the Agulhas Current from space: An assessment of ASAR surface current velocities," *J. Geophys. Res.*, vol. 115, no. C10, pp. 105–109, Oct. 2010.
[9] R. K. Raney, "Wave orbital velocity, fade and SAR response to azimuth waves," *IEEE J. Ocean. Eng.*, vol. OE-6, no. 4, pp. 140–146, Oct. 1981.
[10] A. Jain, "SAR imaging of ocean waves: Theory," *IEEE J. Ocean. Eng.*, vol. OE-6, no. 4, pp. 130–139, Oct. 1981.
[11] W. R. Alpers, D. B. Ross, and C. L. Rufenach, "On the detectability of ocean surface waves by real and synthetic aperture radar," *J. Geophys. Res.*, vol. 86, no. C7, pp. 6481–6498, Jul. 1981.
[12] K. Hasselmann *et al.*, "Theory of synthetic aperture radar ocean imaging: a MARSEN view," *J. Geophys. Res.*, vol. 90, no. C3, pp. 4659–4686, May 1985.
[13] W. R. Alpers and C. Bruening, "On the relative importance of motion-related contributions to the SAR imaging mechanism of ocean surface waves," *IEEE Trans. Geosci. Remote Sens.*, vol. GE-24, no. 6, pp. 873–885, Nov. 1986.
[14] W. R. Alpers, "Monte Carlo simulations for studying the relationship between ocean wave and synthetic aperture radar image spectra," *J. Geophys. Res.*, vol. 88, no. C3, pp. 1745–1759, Feb. 1983.

[15] R. O. Harger and C. E. Korman, "Comparisons of simulated and actual synthetic aperture radar gravity wave images," *J. Geophys. Res.*, vol. 93, no. C11, pp. 13 867–13 882, Nov. 1988.

[16] M. Durand, L.-L. Fu, D. P. Lettenmaier, D. E. Alsdorf, E. Rodriguez, and D. Esteban-Fernandez, "The surface water and ocean topography mission: Observing terrestrial surface water and oceanic submesoscale eddies," *Proc. IEEE*, vol. 98, no. 5, pp. 766–779, May 2010.

[17] T. Börner *et al.*, "SIGNAL: SAR for ice, glacier and global dynamics," in *Proc. IGARSS*, Honolulu, HI, USA, 2010, pp. 2884–2887.

[18] S. Bertl *et al.*, "Ka-band multi-baseline ati-sar system for ocean surface currents measurements," in *Proc. 1st Workshop Ka-Band Earth Observation Radar Missions*, Nov. 2012, pp. 1–8.

[19] M. Younis, P. López-Dekker, A. Patyuchenko, and G. Krieger, "Digital beamforming architecture and techniques for a spaceborne interferometric ka-band mission," in *Proc. IEEE Radar Conf.*, Ottawa, ON, Canada, Apr. 2013, pp. 1–5.

[20] A. Uematsu, R. Nakamura, Y. Nakajima, and Y. Yajima, "X-band Interferometric SAR Sensor for the Japanese Altimetry Mission, COMPIRA," in *Proc. IEEE IGARSS*, Melbourne, Vic., Australia, 2013, pp. 2943–2946.

[21] T. R. Larson, L. I. Moskowitz, and J. W. Wright, "A note on SAR imagery of the ocean," *IEEE Trans. Antennas Propag.*, vol. AP-24, no. 3, pp. 393–394, May 1976.

[22] C. E. Elachi and W. E. Brown, "Models of radar imaging of the ocean surface waves," *IEEE Trans. Antennas Propag.*, vol. AP-25, no. 1, pp. 84–95, Jan. 1977.

[23] C. T. Swift and L. R. Wilson, "Synthetic aperture radar imaging of ocean waves," *IEEE Trans. Antennas Propag.*, vol. AP-27, no. 6, pp. 725–729, Nov. 1979.

[24] G. R. Valenzuela, "An asymptotic formulation for SAR images of the dynamical ocean surface," *Radio Sci.*, vol. 15, no. 1, pp. 105–114, Jan. 1980.

[25] R. O. Harger, "The side-looking radar image of time-variant scenes," *Radio Sci.*, vol. 15, pp. 749–756, 1980.

[26] R. K. Raney, "SAR response to partially coherent phenomena," *IEEE Trans. Antennas Propag.*, vol. AP-28, no. 6, pp. 777–787, Nov. 1980.

[27] A. V. Ivanov, "On the synthetic aperture radar imaging of ocean surface waves," *IEEE J. Ocean Eng.*, vol. OE-7, no. 2, pp. 96–103, Apr. 1982.

[28] R. O. Harger, "SAR ocean imaging mechanisms," in *Spaceborne Synthetic Aperture Radar for Oceanography*, R. C. Beal, P. S. DeLeonibus, and I. Katz, Eds. Baltimore, MD, USA: John Hopkins Univ. Press, 1981, pp. 41–52.

[29] K. Ouchi, "Effect of defocussing on the images of ocean waves," in *Satellite Microwave Remote Sensing*, T. D. Allan, Eds. Chichester, U.K.: Ellis Horwood, 1983, pp. 209–222.

[30] S. Rotheram, "Theory of SAR ocean wave imaging," in *Satellite Microwave Remote Sensing*, T. D. Allan, Eds. Chichester, U.K.: Ellis Horwood, 1983, pp. 155–186.

[31] M. J. Tucker, "The effect of a movin sea surface on SAR imagery," in *Satellite Microwave Remote Sensing*, T. D. Allan, Eds. Chichester, U.K.: Ellis Horwood, 1983, pp. 146–154.

[32] W. J. Plant and W. C. Keller, "The two-scale radar wave probe and SAR imagery of the ocean," *J. Geophys. Res.*, vol. 88, no. C14, pp. 9776–9784, Nov. 1983.

[33] W. R. Alpers, "Imaging ocean surface waves by synthetic aperture radar-A review," in *Satellite Microwave Remote Sensing*, T. D. Allan, Ed. Chichester, U.K.: Ellis Horwood, 1983, ch. 6.

[34] A. V. Ivanov, "On the mechanism for imaging ocean waves by synthetic aperture radar," *IEEE Trans. Antennas Propag.*, vol. AP-31, no. 3, pp. 538–541, May 1983.

[35] K. Ouchi, "Two-dimensional imaging mechanisms of ocean waves by synthetic aperture radars," *J. Phys. D, Appl. Phys.*, vol. 17, no. 1, pp. 25–42, 1984.

[36] M. J. Tucker, "The decorrelation time of microwave echoes from the sea surface," *Int. J. Remote Sens.*, vol. 6, no. 7, pp. 1075–1089, 1985.

[37] R. O. Harger, "The SAR image of short gravity waves on a long gravity wave," in *Wave Dynamics and Radio Probing of the Ocean Surface*, O. M. Phillips and K. Hasselmann, Eds. New York, NY, USA: Plenum, 1986, pp. 371–392.

[38] D. R. Lyzenga, "Numerical simulation of synthetic aperture radar image spectra for ocean waves," *IEEE Trans. Geosci. Remote Sens.*, vol. GE-24, no. 6, pp. 863–872, Nov. 1986.

[39] R. K. Raney and P. W. Vachon, "Synthetic aperture radar imaging of ocean waves from an airborne platform: Focus and tracking issues," *J. Geophys. Res.*, vol. 93, no. C10, pp. 12 457–12 486, Oct. 1988.

[40] D. P. Kasilingam and O. H. Shemdin, "Theory for synthetic aperture radar imaging of the ocean surface: With application to the tower ocean wave and radar dependence experiment on focus, resolution, and wave height spectra," *J. Geophys. Res.*, vol. 93, no. C11, pp. 13 837–13 848, Nov. 1988.

[41] D. R. Lyzenga, "An analytic representation of the synthetic aperture radar image spectrum for ocean waves," *J. Geophys. Res.*, vol. 93, no. C11, pp. 13 859–13 865, Nov. 1988.

[42] P. W. Vachon, R. K. Raney, and W. J. Emery, "A simulation for spaceborne SAR imagery of a distributed, moving scene," *IEEE Trans. Geosci. Remote Sens.*, vol. 27, no. 1, pp. 67–78, Jan. 1989.

[43] D. P. Kasilingam and O. H. Shemdin, "Models for synthetic aperture radar imaging of the ocean: A comparison," *J. Geophys. Res.*, vol. 95, no. C9, pp. 16 263–16 276, Sep. 1990.

[44] C. Brüning, W. R. Alpers, and K. Hasselmann, "Monte-Carlo simulation studies of the nonlinear imaging of a two dimensional surface wave field by a synthetic aperture radar," *Int. J. Remote Sens.*, vol. 11, no. 10, pp. 1695–1727, 1990.

[45] D. P. Kasilingam, H. Davidw, and H. S. Omar, "Focusing of synthetic aperture radar ocean images with long integration times," *J. Geophys. Res.*, vol. 96, no. C9, pp. 16 935–16 942, Sep. 1991.

[46] L. Shemer and E. Kit, "Simulation of an interferometric synthetic aperture radar imagery of ocean system consisting of a current and a monochromatic wave," *J. Geophys. Res.*, vol. 96, no. C12, pp. 22 063–22 073, Dec. 1991.

[47] L. Shemer, "An analytical presentation of the monochromatic ocean wave image by a regular or an interferometric synthetic aperture radar," *IEEE Trans. Geosci. Remote Sens.*, vol. 33, no. 4, pp. 1008–1013, Jul. 1995.

[48] M. Bao, C. Brüning, and W. R. Alpers, "Simulation of ocean waves imaging by an along-track interferometric synthetic aperture radar," *IEEE Trans. Geosci. Remote Sens.*, vol. 35, no. 3, pp. 618–631, May 1997.

[49] G. Franceschetti, M. Migliaccio, and D. Riccio, "On ocean SAR raw signal simulation," *IEEE Trans. Geosci. Remote Sens.*, vol. 36, no. 1, pp. 84–100, Jan. 1998.

[50] G. Franceschetti, A. Iodice, D. Riccio, G. Ruello, and R. Siviero, "SAR raw signal simulation of oil slicks in ocean environments," *IEEE Trans. Geosci. Remote Sens.*, vol. 40, no. 9, pp. 1935–1949, Sep. 2002.

[51] B. Chapron, F. Collard, and F. Ardhuin, "Direct measurements of ocean surface velocity from space: Interpretation and validation," *J. Geophys. Res.-Oceans*, vol. 110, no. C7, Jul. 2005, Art. no. C07008.

[52] M. W. Hansen, F. Collard, K. F. Dagestad, J. A. Johannessen, P. Fabry, and B. Chapron, "Retrieval of Sea Surface Range Velocities From Envisat ASAR Doppler Centroid Measurements," *IEEE Trans. Geosci. Remote Sens.*, vol. 49, no. 10, pp. 3582–3592, Oct. 2011.

[53] G. Franceschetti, M. Migliaccio, D. Riccio, and G. Schirinzi, "SARAS: A Synthetic Aperture Radar (SAR) raw signal simulator," *IEEE Trans. Geosci. Remote Sens.*, vol. 30, no. 1, pp. 110–123, Jan. 1992.

[54] H. J. Song, M. H. Zhu, and Y. T. Bai, "Design of general purpose simulation package of SAR system," in *Proc. Radar*, Edinburg, U.K., 1997, pp. 697–699.

[55] M. Smolarczyk, "Radar signal simulator for SAR algorithm test," in *Proc. IRS*, Dresden, Germany, Sep. 2003, pp. 749–752.

[56] E. Boerner, R. Lord, J. MitterMayer, and R. Bamler, "Evaluation of TerraSAR-X spotlight processing accuracy based on a new spotlight raw data simulator," in *Proc. IGARSS*, Toulouse, France, 2003, pp. 1323–1325.

[57] A. Mori and F. De Vita, "A time-domain raw signal simulator for interferometric SAR," *IEEE Trans. Geosci. Remote Sens.*, vol. 42, no. 9, pp. 1811–1817, Sep. 2004.

[58] M. Vandewal, R. Speck, and H. Süß, "Raw data simulation for SAR-systems on UAV-platforms," in *Proc. EUSAR*, Ulm, Germany, May 2004, pp. 597–600.

[59] L. de Salvador, P. Bemad, A. Fidalgo, G. Ilundain, J. M. Dominguez, and L. Ojalvo, "IFSAR: An airborne interferometric SAR simulator," in *Proc. IGARSS*, Anchorage, AK, USA, 2004, pp. 3349–3352.

[60] F. Comblet, F. Pellen, A. Baussard, and A. Khenchaf, "Bistatic SAR: Theory and simulation," in *Proc. IEEE Antennas Propag. Soc. Int. Symp.*, 2005, vol. 2A, pp. 664–667.

[61] Z. H. Bawar, T. Long, and T. Zeng, "Innovative development of spaceborne InSAR simulator," in *Proc. IEEE Symp. Emerging Technol.*, 2005, pp. 359–364.

[62] Y. Wu, H. Wang, and X. Jia, "Study and simulation on bistatic SAR," in *Proc. 7th Int. Symp. Antennas, Propag. EM Theory*, 2006, pp. 1–4.

[63] S. Zhang, T. Zeng, T. Long, and J. Chen, "Research on echo simulation of space-borne bistatic SAR," in *Proc. CIE Int. Conf. Radar*, 2006, pp. 1–4.

[64] F. Xu and Y. Jin, "Imaging simulation of polarimetric SAR for a comprehensive terrain scene using the mapping and projection algorithm,"

IEEE Trans. Geosci. Remote Sens., vol. 44, no. 11, pp. 3219–3234, Nov. 2006.

[65] Z. Xiang, K. Z. Wang, X. Z. Liu, and W. X. Yu, "A GPU based time-domain raw signal simulator for interferometric SAR," in *Proc. IEEE IGARSS*, Cape Town, South Africa, 2009, vol. 5, pp. 25–28.

[66] F. Zhang, C. Hu, W. Li, W. Hu, and H.-C. Li, "Accelerating time-domain SAR raw data simulation for large areas using multi-GPUs," *IEEE Trans. Geosci. Remote Sens.*, vol. 52, no. 9, pp. 3956–3966, Sep. 2014.

[67] G. Franceschetti, A. Iodice, S. Perna, and D. Riccio, "SAR sensor trajectory deviations: Fourier domain formulation and extended scene simulation of raw signal," *IEEE Trans. Geosci. Remote Sens.*, vol. 44, no. 9, pp. 2323–2334, Sep. 2006.

[68] G. Franceschetti, V. Pascazio, and G. Schirinzi, "A SAR raw data simulator of nonstationary scenes," in *Proc. IEEE IGARSS*, 1990, pp. 2405–2408.

[69] G. Franceschetti, M. Migliaccio, and D. Riccio, "SAR raw signal simulation of actual ground sites described in terms of sparse input data," *IEEE Trans. Geosci. Remote Sens.*, vol. 32, no. 6, pp. 1160–1169, Nov. 1994.

[70] G. Franceschetti, A. Iodice, M. Migliaccio, and D. Riccio, "A novel across-track SAR interferometry simulator," *IEEE Trans. Geosci. Remote Sens.*, vol. 36, no. 3, pp. 950–962, May 1998.

[71] G. Franceschetti, A. Iodice, D. Riccio, and G. Ruello, "A 2-D Fourier domain approach for spotlight SAR raw signal simulation of extended scenes," in *Proc. IGARSS*, 2002, vol. 2, pp. 853–855.

[72] R. Speck, M. Hager, M. Garcia, and H. Süß, "An end-to-end-simulator for spaceborne SAR-systems," in *Proc. EUSAR*, Köln, Germany, Jun. 2002, pp. 237–239.

[73] S. Cimmino, G. Franceschetti, A. Iodice, D. Riccio, and G. Ruello, "Efficient spotlight SAR raw signal simulation of extended scenes," *IEEE Trans. Geosci. Remote Sens.*, vol. 41, no. 10, pp. 2329–2337, Oct. 2003.

[74] G. Franceschetti, A. Iodice, D. Riccio, and G. Ruello, "SAR raw signal simulation for urban structures," *IEEE Trans. Geosci. Remote Sens.*, vol. 41, no. 9, pp. 1986–1995, Sep. 2003.

[75] G. Franceschetti, R. Guida, A. Iodice, D. Riccio, and G. Ruello, "Efficient simulation of hybrid stripmap/spotlight SAR raw signals from extended scenes," *IEEE Trans. Geosci. Remote Sens.*, vol. 42, no. 11, pp. 2385–2396, Nov. 2004.

[76] K. Eldhuset, "Raw signal simulation for very high resolution SAR based on polarimetric scattering theory," in *Proc. IGARSS*, Anchorage, AK, USA, 2004, vol. 3, pp. 1774–1777.

[77] K. Eldhuset, "High resolution spaceborne INSAR simulation with extended scenes," *Proc. Inst. Elect. Eng.-Radar Sonar Navig.*, vol. 152, no. 2, pp. 53–57, Apr. 2005.

[78] A. S. Khwaja, L. Ferro-Famil, and E. Pottier, "SAR raw data generation using inverse SAR image formation algorithms," in *Proc. IEEE IGARSS*, Denver, CO, USA, 2006, pp. 4191–4194.

[79] G. Franceschetti, A. Iodice, S. Perna, and D. Riccio, "Efficient simulation of airborne SAR raw data of extended scenes," *IEEE Trans. Geosci. Remote Sens.*, vol. 44, no. 10, pp. 2851–2860, Oct. 2006.

[80] M. Vandewal, R. Speck, and H. Süß, "Efficient SAR raw data generation including low squint angles and platform instabilities," *IEEE Geosci. Remote Sens. Lett.*, vol. 5, no. 1, pp. 26–30, Jan. 2008.

[81] H. Lu, N. Cao, W. W. Liu, F. Wang, and J. R. Hu, "Efficient SAR raw data simulation of extended scenes using chirp scaling principle," in *Proc. Int. Conf. Inf. Sci. Eng.*, 2009, pp. 554–557.

[82] A. S. Khwaja, L. Ferro-Famil, and E. Pottier, "Efficient SAR raw data generation for anisotropic urban scenes based on inverse processing," *IEEE Geosci. Remote Sens. Lett.*, vol. 6, no. 4, pp. 757–761, Oct. 2009.

[83] B. Deng, Y. L. Qing, H. Q. Wang, X. Li, and Y. P. Li, "Inverse Frequency Scaling Algorithm (IFSA) for SAR raw data simulation," in *Proc. Int. Conf. Signal Process. Syst.*, 2010, vol. 2, pp. 317–320.

[84] X. Qiu, D. H. Hu, L. J. Zhou, and C. B. Ding, "A bistatic SAR raw data simulator based on inverse ω-k algorithm," *IEEE Trans. Geosci. Remote Sens.*, vol. 48, no. 3, pp. 1540–1547, Mar. 2010.

[85] O. Dogan and M. Kartal, "Efficient stripmap-mode SAR raw data simulation including platform angular deviations," *IEEE Geosci. Remote Sens. Lett.*, vol. 8, no. 4, pp. 784–788, Jul. 2011.

[86] A. S. Khwaja, L. Ferro-Famil, and E. Pottier, "Efficient stripmap SAR raw data generation taking into account sensor trajectory deviations," *IEEE Geosci. Remote Sens. Lett.*, vol. 8, no. 4, pp. 794–798, Jul. 2011.

[87] O. Dogan and M. Kartal, "Efficient strip-mode SAR raw-data simulation of fixed and moving targets," *IEEE Geosci. Remote Sens. Lett.*, vol. 8, no. 5, pp. 884–888, Sep. 2011.

[88] C. Cafforio, C. Prati, and F. Rocca, "SAR data focusing using seismic migration techniques," *IEEE Trans. Aerosp. Electron. Syst.*, vol. 27, no. 2, pp. 194–207, Mar. 1991.

[89] I. Cumming and F. Wong, *Digital Processing of Synthetic Aperture Radar Data*. Norwood, MA, USA: Artech House, 2005.

[90] R. H. Stolt, "Migration by transform," *Geophysics*, vol. 43, no. 1, pp. 23–48, Feb. 1978.

[91] D. R. Lyzenga, R. A. Shuchman, J. D. Lyden, and C. L. Rufenach, "SAR imaging of waves in water and ice: Evidence of velocity bunching," *J. Geophys. Res.*, vol. 90, no. C1, pp. 1031–1036, Jan. 1985.

[92] K. Raney, H. Runge, R. Bamler, I. Cumming, and F. Wong, "Precision SAR processing using chirp scaling," *IEEE Trans. Geosci. Remote Sens.*, vol. 32, no. 4, pp. 786–799, Jul. 1994.

[93] J. W. Wright, "A new model for sea clutter," *IEEE Trans. Antennas Propag.*, vol. AP-16, no. 2, pp. 217–223, Mar. 1968.

[94] A. Defant, *Physical Oceanography*, vol. I/II. New York, NY, USA: Pergamon, 1961.

[95] K. Hasselmann *et al.*, "Measurements of wind-wave growth and swell decay during the Joint North sea wave project (JONSWAP)," Deutsche Hydrographische Zeitschrift, Reihe A, Hamburg, Germany, no. 12, pp. 1–95, 1973.

[96] W. J. Plant, "Reconciliation of theories of synthetic aperture radar imagery of ocean waves," *J. Geophys. Res.*, vol. 97, no. C5, pp. 7493–7501, May 1992.

[97] W. J. Plant and D. L. Schuler, "Remote Sensing of the sea surface using one- and two-frequency microwave techniques," *Radio Sci.*, vol. 15, no. 3, pp. 605–615, May 1980.

[98] C. J. Oliver, "Representation of radar sea clutter," *Proc. Inst. Elect. Eng.— F Radar Signal Process.*, vol. 135, no. 6, pp. 497–500, Dec. 1988.

[99] V. Gregers-Hansen and R. Mital, "An improved empirical model for radar sea clutter reflectivity," *IEEE Trans. Aerosp. Electron. Syst.*, vol. 48, no. 4, pp. 3512–3524, Oct. 2012.

[100] S. N. Madsen, "Estimating the Doppler centroid of SAR data," *IEEE Trans. Aerosp. Electron. Syst.*, vol. 25, no. 2, pp. 134–140, Mar. 1989.
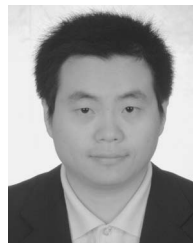
Baochang Liu was born in Shandong, China. He received the B.S. degree in electrical engineering from Liaocheng University, Liaocheng, China, in 2004 and the Ph.D. degree in signal processing from Xidian University, Xi'an, China, in 2010.

He is currently a Lecturer with the School of Marine Sciences, Nanjing University of Information Science and Technology, Nanjing, China. He is the author of over 20 research papers. His research interests include multichannel SAR system design, high-resolution wide-swath SAR, SAR signal processing, moving target indication, and ocean microwave remote sensing.

Yijun He (M'03) received the B.S. degree in physics from Hunan Normal University, Changsha, China, in 1985; the M.S. degree in applied physics from Xidian University, Xi'an, China, in 1990; and the Ph.D. degree in microwave theory and technology from Southeast University, Nanjing, China, in 1993.

He was a Visiting Scientist with the University of Hamburg, Hamburg, Germany; with the Bedford Institute of Oceanography, Dartmouth, NS, Canada; and with the University of Delaware, Newark, DE, USA. From 1993 to 1996, he was a Postdoctoral Fellow with the Ocean Remote Sensing Institute, Ocean University of China, Qingdao, China. From 1999 to 2011, he was with the Key Laboratory of Ocean Circulation and Waves, Institute of Oceanology, Chinese Academy of Sciences, where he was the Head of the Remote Sensing Group and Senior Scientist in satellite oceanography. He is currently a Professor of ocean remote sensing and the Dean of the School of Marine Sciences, Nanjing University of Information Science and Technology, Nanjing, China. His research interests include SAR ocean imaging, ocean-surface current retrieval by multichannel SAR, ocean wave and wind retrieval by fully polarization SAR and other microwave radar at low incidence angle, and sea-surface scattering of electromagnetic waves.